Journal of Hazardous Materials 432 (2022) 128585

Contents lists available at ScienceDirect

Journal of Hazardous Materials

journal homepage: www.elsevier.com/locate/jhazmat

Research Paper

Sources and fate of atmospheric microplastics revealed from inverse and dispersion modelling: From global emissions to deposition

Nikolaos Evangeliou [a,*], Ondřej Tichý [b], Sabine Eckhardt [a], Christine Groot Zwaaftink [a], Janice Brahney [c]

[a] Norwegian Institute for Air Research (NILU), Instituttveien 18, 2007 Kjeller, Norway
[b] The Czech Academy of Sciences, Institute of Information Theory and Automation, Prague, Czech Republic
[c] Department of Watershed Sciences and Ecology Center, Utah State University, Logan, UT 84322, USA

HIGHLIGHTS

- About 9.6 and 6.5 Tg y-1 of microplastics and microfibers 1 are globally released.
- Global average monthly surface MPs (MFs) were 47 ng m-3 (33 ng m-3) at maximum.
- 1.8% of the emitted microplastics from ocean to land, 1.4% from land to ocean.
- Validation suggests that removal of microplastics in global models needs update.
- Results can be used as a proxy of the expected global levels for experimentalists.

GRAPHICAL ABSTRACT

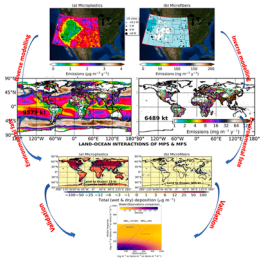

ARTICLE INFO

Editor: Zaher Hashisho

Keywords:
Microplastics
Microfibers
Transport
Dispersion
Airborne contaminants

ABSTRACT

We combine observations from Western USA and inverse modelling to constrain global atmospheric emissions of microplastics (MPs) and microfibers (MFs). The latter are used further to model their global atmospheric dynamics. Global annual MP emissions were calculated as 9.6 ± 3.6 Tg and MF emissions as 6.5 ± 2.9 Tg. Global average monthly MP concentrations were 47 ng m^{-3} and 33 ng m^{-3} for MFs, at maximum. The largest deposition of agricultural MPs occurred close to the world's largest agricultural regions. Road MPs mostly deposited in the East Coast of USA, Central Europe, and Southeastern Asia; MPs resuspended with mineral dust near Sahara and Middle East. Only 1.8% of the emitted mass of oceanic MPs was transferred to land, and 1.4% of land MPs to ocean; the rest were deposited in the same environment. Previous studies reported that 0.74–1.9 Tg y^{-1} of land-based atmospheric MPs/MFs (< 5 mm) are transported to the ocean, while riverine transport is between 3.3 and 14 Tg y^{-1}. We calculate that 0.418 ± 0.201 Tg y^{-1} MPs/MFs (size up to 250 and 2500 μm) were transported from the land to ocean (large particles were ignored). Model validation against observations showed that particle removal must be urgently updated in global models.

* Corresponding author.
E-mail address: Nikolaos.Evangeliou@nilu.no (N. Evangeliou).

https://doi.org/10.1016/j.jhazmat.2022.128585
Received 29 October 2021; Received in revised form 23 February 2022; Accepted 24 February 2022
Available online 26 February 2022

1. Introduction

Since the first reports on the presence of plastic debris in the marine environment in the early 70 s (Carpenter et al., 1972; Carpenter and Smith, 1972; Colton et al., 1974), there has been an increased awareness of plastic accumulation in the environment. The global production of plastics in 2019 reached 368 Mt (from 225 Mt in 2004) (PlasticsEurope, 2019) without PET-fibers (polyethylene terephthalate), PA-fibers (aromatic polyamide) and polyacrylic-fibers included. An estimated 10% of total production is believed to end up in the sea every year by riverine of washout transport (Barnes et al., 2009; Mattsson et al., 2015), although Weiss et al. (2021) recently argued that this might be overestimated. As a result of widespread waste mismanagement, plastic pollution has been confirmed in many freshwater (Blettler et al., 2018), and terrestrial (Chae and An, 2018) ecosystems. Although the majority of plastics exists in the form of macroplastics (>5 mm) (Lebreton et al., 2019), they may fragment into microplastics (MPs, 1 μm to 5 mm) (Peeken et al., 2018) and nanoplastics (NPs, <1 μm) (Wagner and Reemtsma, 2019) via photodegradation, physical abrasion, hydrolysis and biodegradation (Gewert et al., 2015).

MPs have been found in various shapes and sizes in the environment such as 1-D fibers, 2-D fragments (flat particles) and 3-D spherules (Dris et al., 2015). Their origin can be primary, when manufactured in smaller sizes for scientific and medical applications, paint, (Gregory, 1996) or cosmetic products (Fendall and Sewell, 2009) or when originate from abrasion of large plastic objects during manufacturing, use or maintenance (e.g., road dust) (An et al., 2020; Boucher and Friot, 2017; Coyle et al., 2020; Goßmann et al., 2021; Grigoratos and Martini, 2015; Habib et al., 2020; Halle et al., 2020; Hartmann et al., 2019; Jan Kole et al., 2017a; Patil et al., 2021; Sharma and Chatterjee, 2017; Szymańska and Obolewski, 2020; Wang et al., 2018; Yukioka et al., 2020; Zhang et al., 2020). Secondary microplastics are produced by decomposition (O'Brine and Thompson, 2010). The largest portion of the secondary MPs is synthetic microfibers (MFs) produced after washing synthetic clothes (Browne et al., 2011). Athey et al. (2020) reported that a single pair of jeans discharges 56,000 fibers per wash into the wastewater. MFs comprise a range of different shapes, and a widely acceptable nomenclature is missing. Here, we consider MFs as synthetic fibers having a base diameter of less than 10 μm with a height to base diameter ratio of up to 10^3 (J. Liu et al., 2019).

Once MPs are released into the environment, they are subject to physical (e.g. mechanical), radiative, chemical, and biological degradation, which changes their size, shape, surface, composition, and environmental mobility. They become easily airborne following turbulent processes at the surface, similar to dust, not only when they are deposited in continental regions (Qian and Ferro, 2008), but also from the surface of the ocean (Allen et al., 2020), and undergo long-range transport. Airborne MPs will eventually deposit on land or ocean, but may be resuspended again as a result of grasshopping processes (Gouin, 2021). The global atmospheric transport of MPs is generally more efficient than the oceanic or the terrestrial one, as it occurs in much shorter time-scales (weeks compared to years for hemispheric distances, respectively) (Evangeliou et al., 2020; Mountford and Morales Maqueda, 2021). Lately, MPs have been determined in remote regions, from the Alps (Bergmann et al., 2019), the Pyrenees (Allen et al., 2019), and US national parks (Brahney et al., 2020), as far as to Antarctica (González-Pleiter et al., 2020; Kelly et al., 2020) and the high Arctic (Bergmann et al., 2019), whereas modelling reveals atmospheric transport almost everywhere on earth (Evangeliou et al., 2020; Brahney et al., 2021). Notice that presence of MPs in remote regions, distant from major waterways, can result only via the atmosphere.

MPs have been found to affect marine (Wilcox et al., 2018), terrestrial animals (Harne, 2019), and potentially human health (Lehner et al., 2019; Wright and Kelly, 2017), as MPs have been detected in human stool (Schwabl et al., 2019) and all placental portions (Ragusa et al., 2021). Beyond organismal and ecosystem effects, MPs may also influence the global climate indirectly, as enhanced plastic production needs larger consumption of fossil fuels and, in turn, larger emissions (Höök and Tang, 2013; Royer et al., 2018). They also have a direct impact, as MPs are usually colourful and can absorb incoming solar radiation in the atmosphere and where deposited. On snow or ice surfaces, they might decrease surface albedo enhancing melting, similar to conventional pollutants (Hegg et al., 2009). Revell et al. (2021) recently calculated a weak radiative impact, though highlighting that without serious attempts to overhaul plastic production, the abundance and effective radiative forcing of airborne MPs will continue to increase.

Although MPs' role in freshwater, marine and terrestrial ecosystems and biota has been discussed extensively, very little is known on the exact primary and secondary sources and budgets of airborne MPs, due the lack of consistent measurements. Recently, a set of fallout samples from remote and protected areas of the Western USA was collected and analysed for MPs/MFs in both wet and dry atmospheric deposition (Brahney et al., 2020). We make use of these measurements (i) to build a robust methodology that combines atmospheric transport and Bayesian inverse modelling for source quantification; (ii) to calculate emissions of MPs and MFs and determine their main source locations in Western USA. (iii) We calculate global emissions of MPs/MFs by extrapolating regional emissions, and (iv) report on the global dispersion of MPs/MFs calculating the respective budgets from their emissions to the regions they are deposited. Finally, (v) we create a product that comprises the respective levels of surface concentrations and deposition rates in high spatio-temporal resolution (0.5°×0.5°, daily), as a tool for scientists conducting MP/MF measurements to forecast their expected levels.

2. Materials and methods

2.1. Fallout measurements of dry and wet deposition

The detailed methodologies for the determination of MPs and MFs in fallout samples is described in Brahney et al. (2020). Briefly, fallout samples were collected at 11 National Park and Wilderness sites between 2017 and 2019 using Aerochem Metrics model 31 wet/dry collectors (ACMs), which include precipitation sensors that opens the wet bucket, and closes the dry bucket, while precipitation and vice versa. Wet samples were filtered through 0.45 μm polyethersulfone (excluded from the study) filters every week, whereas dry ones were collected at monthly or bi-monthly intervals using custom-built dry sampling units. In total, 236 wet and 103 dry samples were weighed and counted at 100x magnification using a BX50 Olympus Microscope and cellSens Imaging Software and were separated into the following size classes: < 10 μm, 10–25 μm, 25–50 μm, 50–100 μm, 100–250 μm, 250–500 μm, 500–1000 μm, 1000–1500 μm, 1500–2000 μm, 2000–2500 μm, and 2500–3000 μm. Respective densities were assumed between 0.92 and 2.2 g cm^{-3} with a mean of 1.22 g cm^{-3} based on literature values and detected polymers. For justification, mass deposition rates were also estimated using FTIR (Fourier Transform Infra-Red) mapping data, with the limitation that particles < 20 μm cannot be determined. The comparison of the results obtained with both techniques (count-based deposition and FTIR-based deposition showed a strong correlation ($R = 0.89, p < 0.001$) revealing high-quality measurements. As regards to MFs, in subsamples collected, almost all brightly colored particles that fell within the counting criteria described in Brahney et al. (2020) were identified as synthetic using FTIR spectroscopy mapping.

2.2. Atmospheric transport modelling

The source receptor matrices (SRMs) for each fallout sample were calculated with the Lagrangian particle dispersion model FLEXPART version 10.4 (Pisso et al., 2019). The model was driven with 3-hourly operational meteorological wind fields retrieved from the European Centre for Medium-Range Weather Forecasts (ECMWF) consisting of 137 vertical levels and a horizontal resolution of 1°× 1°. The SRMs were

calculated in backwards time (retroplume) mode, using a new feature of FLEXPART that reconstructs wet and dry deposition with backward simulations (Eckhardt et al., 2017). This new feature is an extension of the traditional backward simulation for atmospheric concentrations (Seibert and Frank, 2004). To our knowledge, FLEXPART is the only model with the capability to calculate SRMs of the deposited mass.

More specifically, for the reconstruction of wet deposition of MPs and MFs, computational particles were released at altitudes 0–20 km at the locations of the samples (receptors), as scavenging can occur at any height of the atmosphere, depending on the location of clouds and precipitation. For dry deposition, particles were released at 0–30 m at the respective receptors, as this shallow layer is equal to the height of the layer in which, in forward mode, particles are subject to dry deposition. All released particles represent a unity deposition amount, which was converted immediately (i.e. upon release of a particle) to atmospheric concentrations using the deposition intensity as characterized by either dry deposition velocity or wet scavenging rate (in-cloud and below-cloud scavenging) (Eckhardt et al., 2017; Grythe et al., 2017). The concentrations were then treated as in normal "concentration mode" backward tracking (Seibert and Frank, 2004) to establish SRMs between emissions and deposition amounts (30 d backward tracking). The model output consists of a spatially gridded sensitivity of MPs and MFs deposition at the receptor points to the respective emissions, equivalent to the backwards time mode output for concentrations (Seibert and Frank, 2004). Deposition rates of MPs and MFs (particles m^{-2} d^{-1}) can be computed by multiplying the SRMs (in m) divided with the lowest model layer (100 m) with gridded emissions (particles m^{-2} d^{-1}).

Except for dry and wet deposition (Grythe et al., 2017), FLEXPART accounts for turbulence (Cassiani et al., 2014), unresolved mesoscale motions (Stohl et al., 2005) and convection (Forster et al., 2007). A point that adds uncertainty in our calculations is the efficiency with which particles are scavenged by precipitation. Plastics are generally hydrophobic and should therefore act as inefficient cloud condensation (CCN) or ice nuclei (IN). However, coatings formed during ageing of the aerosols may make the particles more hydrophilic with time (Bond et al., 2013). A recent study by Ganguly and Ariya (2019a) reveals that NPs and MPs may become important for cloud formation and thus anthropogenic climate change. However, since their exact scavenging coefficients are currently unknown, we distinguish between three different in-cloud scavenging properties (low, medium, and high CCN/IN efficiency, Table S1) in each of the aforementioned particle sizes and quantify the uncertainty that is associated with the scavenging efficiency. We adopted the exact particle densities (1.22 g cm^{-3}) and size distribution of MPs and MFs in the model as those reported by Brahney et al. (2020).

2.3. Linear inversion problem and Bayesian inversion

The concept of the SRM is used here assumes that the relationships between the source and the receptor are linear such as that $m_{ij} = c_i/x_j$, where x_j is a hypothetical release from the site in j-th time and c_i is the calculated response at the i-th receptor at the given time period. Then, the measurement, y_i, can be approximated as the sum of the emission, x, weighted by the model predictions, m_{ij}.

The linear equation describing the measurements, $y \in R^p$, based on the modelled SRMs, $M \in R^{p \times n}$, and the unknown release, $x \in R^n$, can be formulated as:

$$y = Mx \tag{1}$$

This formulation can be used for each spatial element as well as for the assumed spatial domain as a whole. We used both these formulations in a two-step procedure to reduce the ill-conditionality of the inversion problem arising when computing spatial distribution of the emission, which is ill-posed problem due to sparse measuring network. First, we solve the inversion problem (Eq. 1) for the whole assumed spatial domain resulting into the estimated source term which is, in essence, averaged emission from each spatial element. Second, we use the emission estimated in the first step as the prior emission for the second step, where the inversion problem (Eq. 1) is solved for each spatial element of the assumed spatial domain. Using this concept, the solution of the second step is more stable and less depends on regularization parameters. Also, to stabilize the inversion, we do not consider measurements that have zero computed concentration by the FLEXPART model for the whole period for a given spatial element, i.e. have zero associated row in the SRM, M.

While the inversion formulation (Eq. 1) appears simple, its solution is non-trivial. Least-squares solution fails due to typically ill-conditioned matrix M in atmospheric problems, due to the associated uncertainties and the nature of the problem (Ganesan et al., 2014; Liu et al., 2017). Therefore, the problem needs to be regularized, i.e. additional information on model parameters or variables needs to be assumed. One such regularization could be the addition of the term $\lambda\|x\|_2^2, \lambda > 0$, to the minimization problem known as the Tikhonov regularization (Golub et al., 1999). When further regularizations are needed, more parameters such as λ are introduced and, notably, need to be set manually or using heuristics (Hansen and O'Leary, 1993). This is, however, also the case of the present inversion problem. In order to reduce manual tuning, we follow the Bayesian formalism, in which the least-squares minimization arising from Eq. 1 can be equivalently formulated as the maximization of the logarithm of Gaussian distribution:

$$arg_x min\|y - Mx\|_2^2 \Longleftrightarrow arg_x max\left(lnN\left(Mx, I_p\right)\right) = arg_x max\left(\frac{-1}{2}\|y - Mx\|_2^2\right) \tag{2}$$

Therefore, the Gaussian distribution $N\left(Mx, I_p\right)$ on the right side of the Eq. 2 is chosen as the prior observation model. Similarly, all other regularization terms can be included in the forms of prior distributions. These prior distributions, appropriately chosen, can form hierarchical priors for all the unknown variables of the inverse model. The key advantage of the Bayesian formalism is that all variables and regularization terms are estimated within the method.

We follow the variational Bayesian methodology (Smidl and Quinn, 2006), in which the posterior distributions of the parameters remain in the same form as their prior distributions. Following Eq. 2, the residual model of y is formulated as the Gaussian distribution with mean value of Mx and an unknown scalar precision of the noise parameter ω as below:

$$p(y|\omega, x) = N\left(Mx, \omega^{-1} I_p\right) \tag{3}$$

$$\propto exp\left(\frac{-1}{2}\omega^{-1}\|y - Mx\|_2^2\right) \tag{4}$$

where $\propto$ denotes equality up to the normalizing constant. For tractability of the model, the prior distribution of the parameter ω is chosen conjugate to the observation model in Eq. 3 using Gamma distribution as follows:

$$p(\omega) = G(\vartheta_0, \rho_0) \tag{5}$$

where ϑ_0 and ρ_0 are scalar constants, which are set to non-informative values 10^{-10} and serve for numerical stabilization in the resulting algorithm to avoid division by zero, when necessary.

The prior model for the source term is based on principles of the LS-APC (least squares with adaptive prior covariance) model (Tichý et al., 2016), in which the emission is assumed to alter between sparse or smooth character, modified using the assumption of the prior source term here. The prior emission term x_0 could be a zero vector, as in the first step for overall emission from the whole domain where no prior information is available, or non-zero, as in the second step where the estimated emission from the first step is used as the prior emission term for each spatial element. The prior distribution of the emission is chosen

as a Gaussian distribution truncated to the positive values with mean vector x_0 and precision (inverse covariance) matrix, Ξ, as:

$$p(x|\Xi) = tN\left(x_0, \Xi^{-1}, [0, +\infty]\right) \quad (6)$$

where the precision matrix, Ξ, is in the specific form of Cholesky decomposition as $\Xi = LVL^T$. The matrix $V = diag(v)$ is the diagonal matrix favouring sparse, i.e. zero, solution(Tipping, 2001), whereas the matrix L is the lower bi-diagonal matrix with ones on diagonal and vector $l \in R^{n-1}$ on sub-diagonal, such as:

$$L = \begin{pmatrix} 1 & 0 & \cdots & \cdots & 0 \\ l_1 & 1 & 0 & \cdots & \vdots \\ 0 & l_2 & \ddots & \ddots & \vdots \\ \vdots & 0 & \ddots & 1 & 0 \\ 0 & 0 & 0 & l_{n-1} & 1 \end{pmatrix} \quad (7)$$

Following Tipping (2001), we select the prior distribution for the introduced variables, vectors v and l as below:

$$p(v_j) = G(\alpha_0, \beta_0), j = 1, \ldots, n \quad (8)$$

$$p(l_j|\psi_j) = N\left(-1, \psi_j^{-1}\right), j = 1, \ldots, n-1 \quad (9)$$

$$p(\psi_j) = G(\zeta_0, \eta_0), j = 1, \ldots, n-1 \quad (10)$$

where the prior constants α_0, β_0, ζ_0, and η_0 are selected again to serve for numerical stability. The prior model of the variable l in Eq. 9, favours a smooth solution using prior mean value of -1 and an unknown variance vector ψ.

Variational Bayes method (Smidl and Quinn, 2006) seeks for approximation of posteriors distribution in the form of conditional independence distribution, so that:

$$p(x, v, l, \psi, \omega|y) \approx \widetilde{p}(x|y)\widetilde{p}(v|y)\widetilde{p}(l|y)\widetilde{p}(\psi|y)\widetilde{p}(\omega|y) \quad (11)$$

The best possible solution minimizes the Kullback-Leibler divergence (Kullback and Leibler, 1951) between the posterior and the hypothetical true posterior as follows:

$$\widetilde{p}(\theta_i|, y) \propto exp\left[E_{\widetilde{p}(\theta_{-i}|, y)} ln(p(\theta, y))\right] \quad (12)$$

where θ_i denotes the i-th variable from the set $\{x, v, l, \psi, \omega\}$ and θ_{-i} denotes complement of θ_i in θ. More details on the method and its implementation can be found in Tichý et al. (2020).

2.4. Extrapolation on a global domain

To extrapolate our estimates in a global domain, we used global datasets of the main sources for MPs and only population density for MFs. Specifically for MPs, global emission inventories of mineral dust, road dust, sea salt, and agriculture were used as the main sources of MPs (Brahney et al., 2021; Chen et al., 2020; Evangeliou et al., 2020; Piehl et al., 2018). Mineral dust emissions were calculated using the FLEXDUST model (Groot Zwaaftink et al., 2017). Road dust emissions were adopted from ECLIPSEv6 emission inventory and are the same as those used in (Evangeliou et al., 2020). Sea salt emissions were taken from (Grythe et al., 2014) as the average emissions from 20 models. Agricultural activities are represented by a global dataset of croplands and pastures developed by combining agricultural inventory data and satellite-derived land cover data (Ramankutty et al., 2008). For MFs, we assumed that their main source is from clothing and should be therefore linked with the distribution of the global population (Henry et al., 2019; O'Brien et al., 2020), which we adopted from NASA (Gao, 2017; Jones and O'Neill, 2016).

For each global emission inventory serving as source of MPs, we computed the average value in our spatial inversion domain, separately for land (cropland, dust, road dust, and population) and oceanic sources (sea salt). Also, we calculated the average posterior release of MPs in our inversion domain for every day. Then, we took their ratio, which we used to calculate global emissions of MPs based on our estimates for each inventory and particle size class with daily temporal resolution. Since the proportion of each MP source to the total emissions is unknown, we assumed different proportions of agricultural, dust, road dust and sea-salt, respectively, that constitute the MPs emissions (see Table S2).

As reported earlier, we assumed that MFs are linked with population density owing its presence to clothing. Hence, in the same way as for MPs, we computed the average population in the studied domain and calculated the ratio with MF releases for every day. Using this ratio and the global population density, we extrapolated our Western USA MF emissions in a global grid for each particle size class with daily temporal resolution.

3. Results

3.1. Annual posterior emissions of microplastics and microfibers in the Western USA

The annual posterior emissions of MPs and MFs can be seen in Fig. 1a and c for the inversion domain (124–91°W, 29–47°N). The calculated daily posterior emissions can be of primary (direct emissions) or secondary origin (emissions from resuspension of previously deposited material). In total, 22 ± 10 million MPs m^{-2} y^{-1} were estimated in five different sizes (5–10 μm, 10–25 μm, 25–50 μm, 50–100 μm, 100–250 μm) following the measured size distribution. The later together with the respective measured densities (average: 1.22 g cm^{-3}) and volume of each size bin gave a total annual emitted mass of MPs of 9.0 ± 3.8 kt y^{-1} in the inversion domain. MF number emissions were in the same order as MPs (24 ± 11 million MFs m^{-2} y^{-1}), albeit they were measured in much larger sizes of up to 2500 μm (Brahney et al., 2020). An accurate conversion of number to mass emissions of MFs is practically impossible, due to the chaotic shape of fibers. The most realistic approach to resemble their capillary shapes would be to assume they are thin cylinders. Here, we distinguish between three different base diameters, all below 10 μm as defined in Liu et al. (2019) (1 μm for MF size 10–25, 25–50, and 50–100 μm; 5 μm for MF size 100–250 μm, 250–500 μm, 500–1000 μm; 10 μm for MF size 1000–1500 μm, 1500–2000 μm, 2000–2500 μm, and 2500–3000 μm). The relevant equations can be found in Supplementary Information. Then, adopting the measured sizes and their respective densities, we calculated a total emitted mass of 244 ± 129 kt y^{-1}. This number is much smaller than the respective for MPs, in contrast to the particle number emissions, because fibers have a much smaller volume than particles. For both MPs and MFs, the calculated mass emitted was higher for larger sizes, although greater number emissions were found at smaller sizes.

Fig. 1b and d show the Taylor diagrams of the mismatches between deposited number concentrations and reconstructed modelled concentrations of MPs and MFs for each size bin. An accurate validation of the posterior emissions requires observations that were not included in the inversion (independent observations). However, the small number of deposition measurements that were available to perform the inversion prevents us from using independent observations from Brahney et al. (2020) here. Hence, the comparison shows only the posterior deposited concentration mismatches to the observations simulated with FLEXPART for any given size bin. For almost all size bins, the Pearson's correlation coefficient was 0.4 – 0.6, while the normalised root mean square error (RMSE) and standard deviation were kept low both for MPs and MFs (Fig. 1).

The spatial distribution of the MP and MF emissions in the Western USA can be seen in Fig. 2 for all size classes and in for each size class. The lowest emissions were calculated close to the measurement stations opposite to the respective footprint emission sensitivity (SRM), which were the highest closer to the measurements (Supplementary Figure S3).

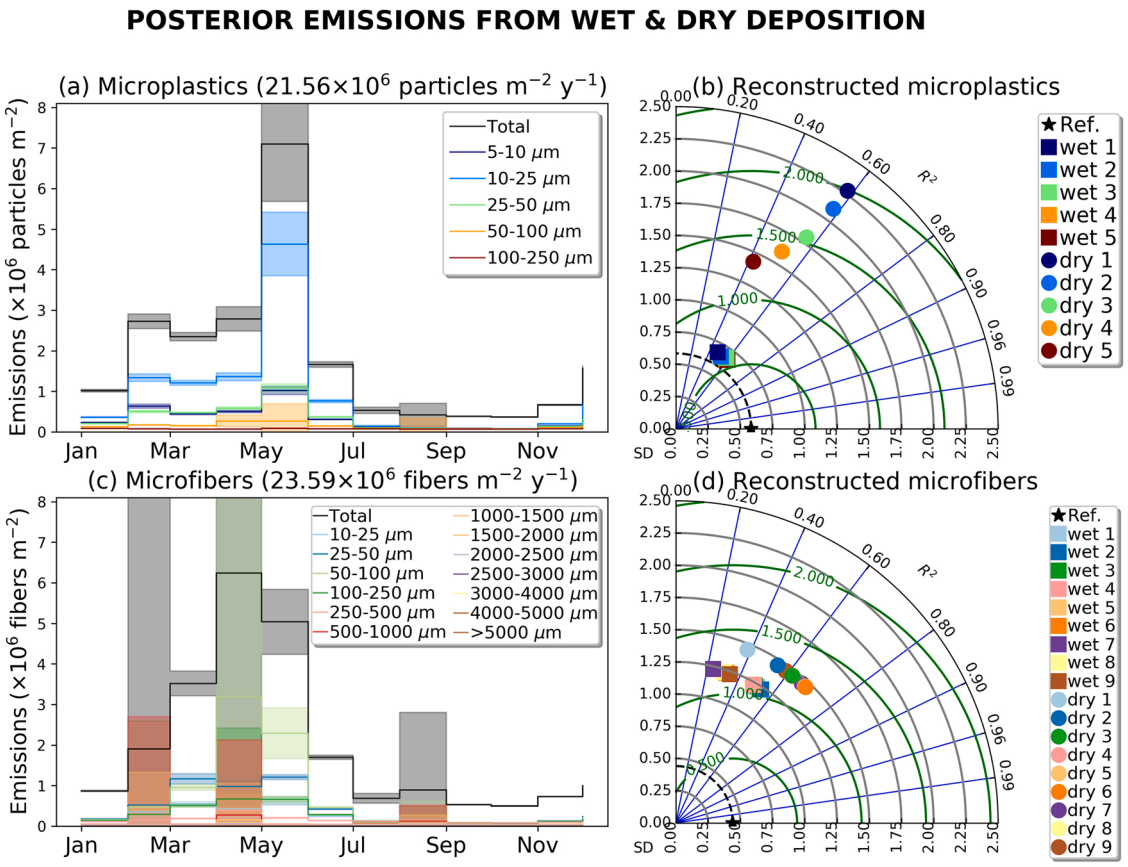

Fig. 1. (a) Posterior monthly emissions of MPs calculated using wet and dry deposition measurements in Western USA. Five different sizes were considered following a measured size distribution, which resulted in total annual MPs emissions of 21.6 million particles m^{-2}. (b) Modelled deposition of MPs against observations both for dry and wet samples for each of the five sizes presented in a Taylor diagram. The latter shows the Pearson's correlation coefficient (gauging similarity in pattern between the modelled and observed deposition) that is related to the azimuthal angle (blue contours); the standard deviation of modelled deposition is proportional to the radial distance from the origin (black contours) and the centered normalised RMSE of modelled deposition is proportional to the distance from the reference standard deviation (green contours). (c) Posterior monthly emissions of MFs in Western USA for nine sizes resulting in an annual total of 23.6 million fibers m^{-2}. (d) Taylor diagram modelled versus observed deposition of MFs both for dry and wet samples for each of the nine sizes.

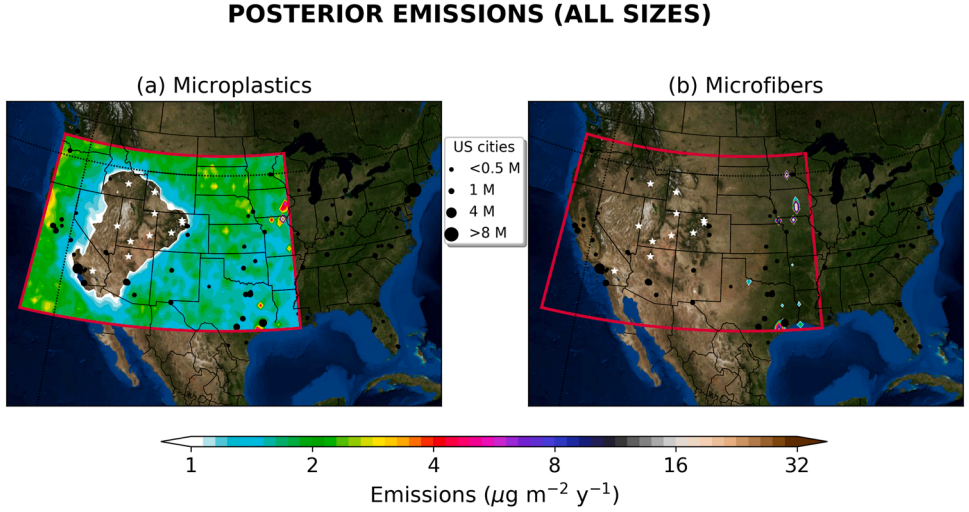

Fig. 2. Spatial distribution of MP and MF emissions in the Western USA calculated from deposition measurements and Bayesian inverse modelling. The largest cities are shown in black circles and the measurement stations in white stars. Note that emissions are stronger away from the stations due to the remote location of the measurement stations away from artificial sources.

This behavior can be expected considering that the measuring stations are located in US national parks and remote areas (45–300 km from urban centers and at elevations ranging from 1240 to 3520 m above sea level), thus, far from any man-made activity that would emit MPs and MFs. On the other hand, our findings are necessarily biased by the remoteness of measurement sites showing the need for sample collection

also close to populated areas.

3.2. Global emissions of microplastics and microfibers

The exact composition of atmospheric MPs from individual sources is currently under uncertain. What is known with some certainty is that primary MPs are estimated to represent between 15% and 31% of MPs in the oceans (Boucher and Friot, 2017). Accordingly, Brahney et al. (2020) determined that 10% of the counted microplastics were primary microbeads. Secondary MPs account for 69–81% of oceanic MPs mostly originating from degradation of larger plastic objects, such as plastic bags, bottles or agricultural or fishing nets (World Economic Forum, 2016). In the present study, MPs were assumed to be produced by road dust (primary source), mineral dust (secondary source), agriculture (secondary source) and sea salt (secondary source), although other sources might be also important (e.g., direct emissions from industrial regions). We give 23% (average of 15 – 31%) to primary sources (in our case, road dust) and we split the rest to all the other secondary sources (mineral dust, agriculture, sea salt) forming 30 scenarios as indicated in Table S2. Their average was used as the basis for the calculation of the MP emissions. MFs have been calculated separately assuming that they only originate from the average population.

The global annual posterior emissions of MPs and MFs can be seen in Fig. 3. For the MPs, emissions were estimated to be 9.6 ± 3.6 Tg y^{-1}, 10% larger than those of Brahney et al. (2021) (8.7 Tg y^{-1}). The calculated global annual emissions per source, size and region can be seen in Table 1. The ocean dominates atmospheric emissions with 8.9 ± 3.5 Tg y^{-1}, as the insoluble plastic debris accumulates at the surface of the ocean and can be resuspended by bubble bursts similar to other sea spray aerosols (Allen et al., 2020). It is slightly higher than that of (Brahney et al., 2021) (8.6 Tg y^{-1}), albeit it shows a completely different distribution, because of the 20 member ensemble used for its calculation. However, it should be noted that the selected inversion domain sufficient to accurately constrain MP emissions covers a very small oceanic surface and any interpolation might be uncertain. Furthermore, the deposition measurements used in the inversion (Brahney et al., 2020) are far from the ocean and the footprint emission sensitivities very weak () inducing an additional uncertainty. A good example for the latter is the part of the Atlantic Ocean and the Gulf of Mexico, where footprint emission sensitivities are very low. For more accurate emission calculations, oceanic stations measuring MPs is a necessity. Agricultural activities resuspend around 0.31 ± 0.13 Tg y^{-1} of plastics previously deposited in the soil (Nizzetto et al., 2016) or from the use of agricultural mulch (Fakour et al., 2021). Road dust contributed another 0.28 ± 0.12 Tg y^{-1}, almost three times higher than in Brahney et al. (2021) (0.096 Tg y^{-1}), and similar to Evangeliou et al. (2020) (0.43 Tg y^{-1}, range: 0.20–1.1 Tg y^{-1}) for tire wear (TWPs) and brake wear particles (BWPs) of size < 10 μm. TWPs are produced by shear forces between the tread and the

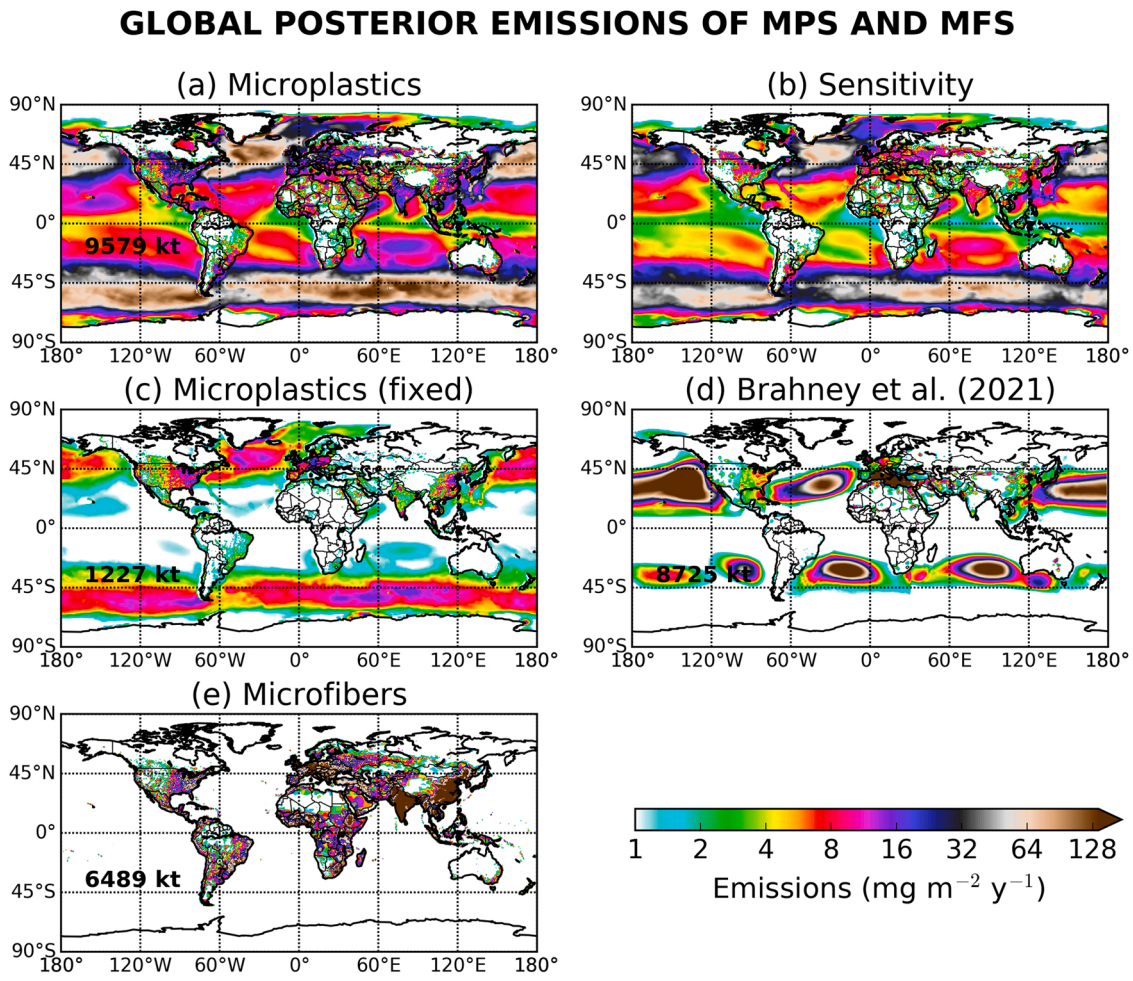

Fig. 3. (a) Annual emissions of MPs revealed from inverse modelling in the Western USA and then extrapolated globally. (b) Sensitivity of the MP emissions to different emission sources (road dust, mineral dust, agricultural activity, and sea salt). The sensitivity is calculated here as the standard deviation of the 30 different scenarios that consider different proportions of emission sources with respect to total MP emissions (Table S2). (c) Global annual MP emissions calculated with the source proportions described in (Brahney et al., 2021) (Table S1). (d) Global annual MP emissions from (Brahney et al., 2021). (e) Annual emissions of MFs revealed from inverse modelling in the Western USA and then extrapolated globally.

Table 1
Global annual emissions of MPs and MFs (in Tg y^{-1}) per different source, size and region (according to Supplementary Figure S4).

Tg y^{-1}	RD	DU	AG	SS	PO	Total
MPs	0.28±0.12	0.10±0.052	0.31±0.13	8.9±3.5		9.6±3.6
MPs (Brahney et al., 2021)	96×10^{-3}	68×10^{-3}	18×10^{-3} *	8.6	0.0	8.7
MFs					6.5±2.9	6.5±2.9

Tg y^{-1}	5–10 μm	10–25 μm	25–50 μm	50–100 μm	100–250 μm	250-500 μm	500-1000 μm	1000-1500 μm	1500-2000 μm	2000-2500 μm
MPs	7.9±3.1×10^{-3}	0.11±0.05	0.50±0.23	2.0±0.92	7.3±3.0					
MPs (Brahney et al., 2021)	6.2×10^{-2}	1.4×10^{-1}	1.1	7.4	-					
MFs		3.9±1.5×10^{-5}	2.9±0.91×10^{-4}	1.4±0.5×10^{-3}	6.7±2.8×10^{-3}	1.4±0.6×10^{-2}	3.1±1.5×10^{-2}	2.9±1.1	1.9±1.0	1.6±0.8

Tg y^{-1}	Asia	Russia	Greenland	Europe	N. America	C. America	S. America	Africa	Oceania	Antarctica	Ocean	Total
MPs	0.25±0.12	44±20×10^{-3}	0.18±0.95×10^{-3}	88±42×10^{-3}	0.13±0.055	15±7.8×10^{-3}	45±22×10^{-3}	0.11±0.055	12±5.8×10^{-3}	9.0±4.6×10^{-5}	8.9±3.5	9.6±3.6
MPs (Brahney et al., 2021)	88×10^{-3}	2.3×10^{-3}	12×10^{-5}	49×10^{-3}	24×10^{-3}	3.1×10^{-3}	7.1×10^{-3}	9.3×10^{-3}	3.9×10^{-3}	9.8×10^{-8}	8.6	8.7
MFs	3.7±1.3	0.44±0.25	4.7±1.4×10^{-2}	0.46±0.14	0.28±0.12	0.18±0.067	0.52±0.25	0.97±0.45	0.051±0.024	2.3±1.0×10^{-5}	0	6.5±2.9

*described as dustpop in Brahney et al. (2021).

road pavement (Rogge et al., 1993) or by volatilization (Wagner et al., 2018), and the whole wearing process depends on the type of tire, the road surface, different vehicle characteristics, the state of operation and overall condition of the vehicle (Grigoratos and Martini, 2014). BWPs are produced via mechanical abrasion and corrosion (Penkała et al., 2018; Sommer et al., 2018). Jan Kole et al. (2017b) reported global emissions of TWPs to be about 6.1 Tg y^{-1} (BWP emissions add another 0.5 Tg y^{-1}) not specifying any size range. However, they reported that 3–7% of the PM2.5 (1.2 – 2.8 Tg y^{-1}), is estimated to consist of tire wear and tear. The emissions reported here are one order of magnitude lower. MPs resuspended with mineral dust are the least important (0.10 ± 0.052 Tg y^{-1}) in close agreement with Brahney et al. (2021) (0.068 Tg y^{-1}). If the proportion of different sources to total are to be used from Brahney et al. (2021), as reported for deposition (see Table S2), the total emitted MPs are one quarter (~2.4 Tg y^{-1}) of those presented here (9.6 Tg y^{-1}) (Fig. 3c).

As regards to MF emissions (Table 1), the global annual mass emitted was 6.5 ± 2.9 Tg y^{-1} assuming that the only source was fibers from human clothes. Emissions increased with fiber size with a peak at 1000–1500 μm (2.9 ± 1.1 Tg). Gavigan et al. (2020) estimated that 5.6 Tg of synthetic MFs were released from apparel washing between 1950 and 2016, half of it during the last decade, though not specifying what fraction might become airborne. Godfrey (2021) reported that about 0.12 Tg y^{-1} of synthetic MFs are released into the environment annually at the pre-consumer stage, or one shirt for every 500 manufactured. This means that this number rises after accounting for the MF loss at the consumer stage. The total atmospheric emissions calculated in the present study are at least an order of magnitude higher.

The continental distribution of the calculated MP and MF emissions can be seen in Table 1 calculated using continental masks as defined in. Due to the lack of emission data, the only comparison can be performed against the emissions calculated by Brahney et al. (2021). The annual total MP emissions in Asia were estimated to be 0.25 ± 0.12 Tg y^{-1} (MF: 3.7 ± 1.3 Tg y^{-1}), in contrast to 0.089 Tg y^{-1} in Brahney et al. (2021). North America contributes another 0.13 ± 0.055 Tg y^{-1} (0.024 Tg y^{-1} in Brahney et al., 2021) (MF: 0.28 ± 0.12 Tg y^{-1}), and Africa 0.11 ± 0.055 Tg y^{-1} (0.093 Tg y^{-1} in Brahney et al., 2021) on MP emissions (MF: 0.97 ± 0.45 Tg y^{-1}). Europe (MPs/MFs: 0.088 ± 0.042/0.46 ± 0.14 Tg y^{-1}) emits twice as much MPs as Russia (MPs/MFs: 0.044 ± 0.020/0.44 ± 0.25 Tg y^{-1}) or South America (MPs/MFs: 0.045 ± 0.022/0.52 ± 0.25 Tg y^{-1}), while the rest of the continents have smaller shares in the annual emissions of MPs and MFs. Brahney et al. (2021) calculated MP emissions in Europe to be 0.048 Tg y^{-1}, 0.0023 Tg y^{-1}only in Russia and 0.0071 Tg y^{-1} in South America.

3.3. *Atmospheric transport and deposition*

The global atmospheric transport of MPs emitted from agricultural sources, with mineral and road dust and with sea spray, as well as MFs from the global population can be seen in Video 1 and 2. In the latter, transport is shown in daily temporal resolution for the year of the inversion (2018). The large size of the particles modelled (up to 250 μm

for MPs and 2500 μm for MFs), following the observations used in the inversion, do not present long-range transport characteristics. The latter is reinforced by the assumption that the emissions took place at the surface (within the first 10 m), thus they are not lofted significantly high enough to be transported over longer distances, but they are rather removed fast. Their lifetimes depend not only on the size, but also from how fast they are scavenged by rain droplets and, in turn, removed from the atmosphere (Evangeliou et al., 2020). Here, we have assumed a modelled CCN/IN efficiency to be moderate (Table S1). Hence, for the smallest particles (<10 μm), the lifetime is 8.3 ± 1.0 days and drops with increasing size until 2.5 ± 1.1 days for the largest size (100–250 μm). The same characteristics are also seen for the MFs (Video 2), which were modelled as particles. Although this is inaccurate, as their shape is rather capillary causing different aerodynamic properties, it only gives an indication of how far from the main land sources they should be expected. Their sizes were somewhat higher than those of MPs (15–5000 μm). Nevertheless, particles larger than 2500 μm were not determined, which means that they are removed from the atmosphere so fast that cannot travel at all. This is in agreement with the calculated modelled lifetimes for MFs that were found to be < 2 days for sizes above 500 μm.

Global mean concentrations of MPs and MFs at the surface of the atmosphere can be seen in Fig. 4. Average monthly mass concentrations of MPs ranged between 6 and 47 ng m^{-3} or between 1 and 8 particles m^{-3} d^{-1}, if density and different volume for each size bin are to be considered. MF surface monthly mass concentrations were significantly lower (2.4–33 ng m^{-3}) and daily number concentrations a few fibers m^{-3}. Both for MPs and MFs, one can immediately notice the very rapid removal from the atmosphere, because of the extremely large sizes that were considered in the present. Although larger particles are rarer (Fig. 1), they are much heavier and subsequently removed faster having lifetimes < 1 day. This is shown by almost constant day-to-day variation of daily concentrations in each month, which rather fail to accumulate with time in the atmosphere. Considering that MPs/MFs emissions occur near the surface and are characterized by large sizes, concentrations decline substantially at higher altitudes of the planetary boundary layer (PBL) or in the free troposphere. We calculate that global average daily concentrations of MPs in the PBL to be 1.7–13 times lower (for particle diameters of 5–10 μm and 100–250 μm) than at surface, while in the free troposphere 8–400 times lower (for particle diameters of 5–10 μm and 100–250 μm) than at surface. For MFs, PBL concentrations are 2.5–16 times smaller (for fiber heights between 10 and 25 μm and 2000–2500 μm) than at surface, and free tropospheric concentrations between 9 and 1000 times (for fiber heights between 10 and 25 μm and 2000–2500 μm) smaller than at surface.

The global annual deposition for each MP source (agricultural activities, road and mineral dust, and sea spray) is illustrated in Fig. 5 together with the respective one for MFs. As expected, all the emitted mass has been deposited by the end of the simulation year, while maximum deposition occurred near the largest sources indicating limited transport, because of the large particle/fiber sizes. The largest MPs deposition originating from agricultural sources (annual deposition: 310 ± 131 kt y^{-1}) was seen in Central USA, in the Indo-Gangetic Plain and the North China Plain (Fig. 5a), which are well-known regions of agricultural emissions and have been quantified as the most important sources of agricultural ammonia (Evangeliou et al., 2021). Road MP annual deposition (mainly TWPs and BWPs) was equal to 279 ± 125 kt y^{-1}, with the largest deposition occurring in the East Coast of the USA, Central Europe, and Southeastern Asia (Fig. 5b). Secondary MPs were assumed to be resuspended with mineral dust deposited mainly near Sahara and Middle East (Fig. 5c) with a total annual deposition to be 100 ± 52.2 kt y^{-1}. Similar patterns were calculated for MPs remobilized with sea spray, which deposited mostly in the Ocean (Fig. 5d). The observed MF deposition complies with the general population density, with maxima in Beijing (China) and the Indo-Gangetic Plain (Fig. 5f).

The observed deposition of MPs and MFs in different continental and oceanic regions (according to Fig. S 4) can be found in Table 2. The deposition in different continents mainly originates from the land-based sources (agriculture, transportation, mineral dust), while those in oceanic regions mainly from sea spray. The largest continental annual MP deposition occurred in Asia (267 ± 121 kt y^{-1}), followed by North America (160 ± 71.1 kt y^{-1}), Africa (114 kt y^{-1}) and Europe (102 ± 45.4 kt y^{-1}). The largest continental deposition of MFs occurred in Asia (3792 ± 1933 kt y^{-1}), Africa (801 ± 372 kt y^{-1}) and Europe (598 ± 253 kt y^{-1}), whereas another 846 ± 209 kt y^{-1} were deposited over the American continent. As regards to deposition over the ocean, about 1718 ± 899.5 kt y^{-1} were deposited in the Atlantic Ocean, 2751 ± 1225 kt y^{-1} in the Pacific, 1435 ± 765.5 kt y^{-1} in the Indian and 2289 ± 1185 kt y^{-1} in the Southern Ocean, while deposition in the Mediterranean Sea was one order of magnitude less (102 ± 55.6 kt y^{-1}). The oceanic deposition of MFs was tiny for two reasons, (a) MF emissions were calculated to be negligible in oceanic regions of the inversion domain (see Fig. 2b), hence no emissions from sea spray could be assumed and, subsequently, no direct deposition to the ocean was simulated; (b) the sizes of MFs was very large (see Section 2.1) and no significant transport from the land could be expected.

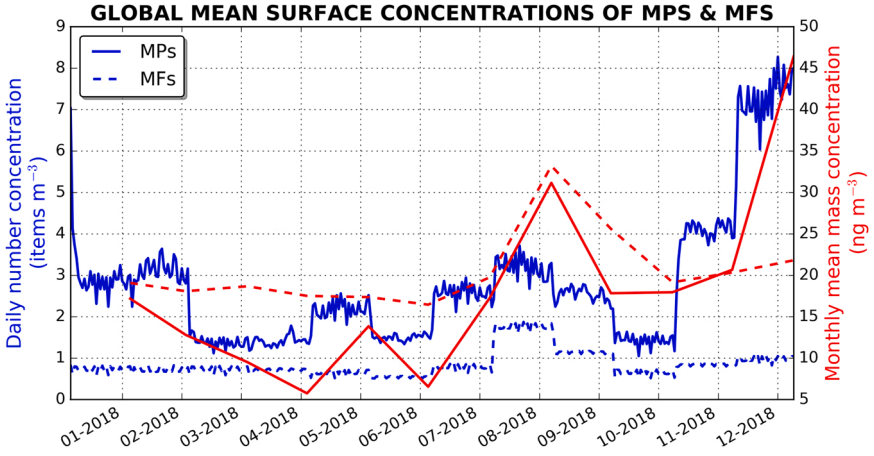

Fig. 4. Timeseries of global mean daily number (blue) and monthly mass (red) concentrations of MPs and MFs at the surface of the atmosphere (0–100 m). The latter can be used as a proxy for the expected surface atmospheric levels by researchers conducting MP measurements.

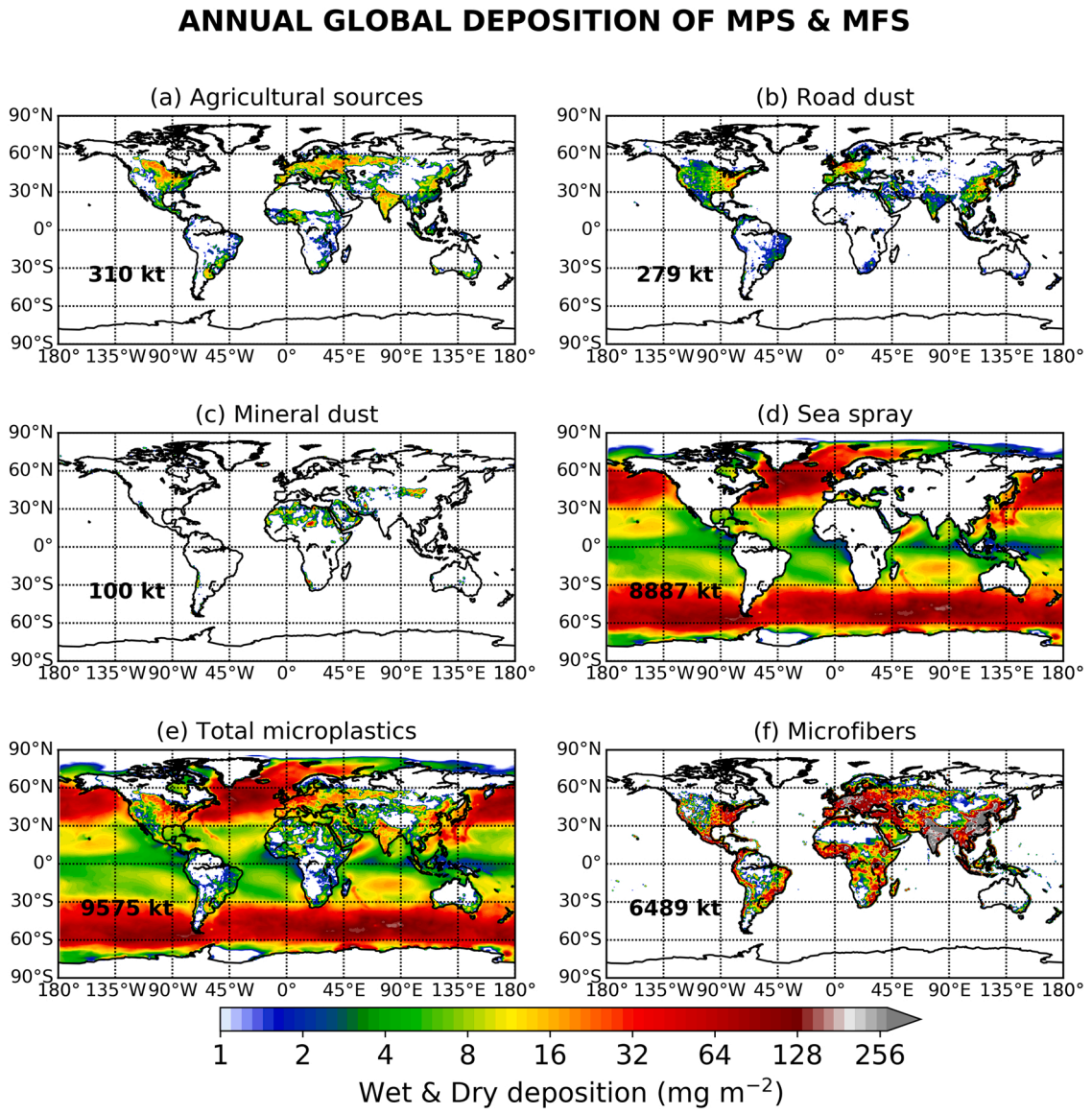

Fig. 5. Annual global deposition of MPs emitted from agriculture, with road and mineral dust and with sea spray. The annual global deposition of MFs from the global population is also given in the lower right panel.

Table 2
Global annual deposition of MPs and MFs (in kt y^{-1}) in different continental, mountainous and oceanic regions (as defined in Supplementary Figure S4).

kt y^{-1}	Asia	Russia	Greenland	Europe	N. America	C. America	S. America	Africa	Oceania	Antarctica	Arctic
MPs	267±121	66±29	5.8±2.5	102±45.4	160±71.1	18±7.8	57±29	114±59	6.8±3.2	8.6±4.4	6.1±3.0
MFs	3792±1933	165±85.5	3.5±1.3	598±253	337±133	160±94.9	349±131	801±372	253±116	47±25×10^{-3}	41±13

kt y^{-1}	Alps	Himalayas	Iceland	Atlantic Ocean	Pacific Ocean	Indian Ocean	Southern Ocean	Mediterranean Sea	Baltic Sea	Black Sea	China Sea
MPs	3.4±1.5	2.1±1.1	1.7±0.55	1718±899.5	2751±1225	1435±765.5	2289±1185	102±55.6	1.4±0.55	0.96±0.45	2.5±1.2
MFs	26±12	79±39	0.24±0.12	16±0.83	8.3±4.6	3.2±1.8	2.7±1.6×10^{-3}	19±8.9	0.39±0.14	0.71±0.36	5.1±×10^{-3}

4. Discussion

4.1. Uncertainty of the posterior emissions in the Western USA

The calculation of the uncertainty of the posterior emissions was performed in two different ways to show the robustness of the methodology used in the present study. The first method is based on a sensitivity study with an ensemble of inversion algorithms employing different scavenging characteristics for MPs and MFs; the uncertainty was calculated as the standard deviation of the different posterior emissions. The different members of the ensemble were built from three different inversion algorithms. The first is the one already described in Section 2.3; the second algorithm is a modification of the first one with the choice of the mean value of prior emissions to be equal to zero ($x_0 = 0$) in Eq. (7). This choice leads to lower estimates since zeros are assumed when no information on releases can be calculated from the observations, which may cause biased estimates. The third algorithm is another version of the first one, where the prior mean value in Eq. (6) is assumed again to be zero ($x_0 = 0$). Moreover, we remove the assumption of not considering measurements that have zero computed SRM sensitivities (calculated with FLEXPART) for the whole studied period in each spatial element. This is a very demanding case, since these measurements do not contribute to the reconstruction of the posterior emissions; however, they remain in the loss function (Eq. 2), which results in a less stable solution with larger emissions. For each of the three inversion algorithms, three different MP and MF species were assumed, each with a different CCN/IN efficiency (Table S1), which gives a total of nine ensemble members for each size of MPs and MFs.

The second method for calculating uncertainty of the posterior emissions in the Western USA is based on the relation between measurement and reconstruction (Eq. 1). In Eq. (1) many types of uncertainties affect the results. For instance, measurements are affected by the spatial and temporal quality of the monitoring network (in addition to the uncertainty of the measurement methodology), i.e., sparse network can significantly bias the results (De Meutter et al., 2020). On the other hand, SRMs accumulate all the biases of the respective atmospheric transport model parametrizations and the uncertainties of the meteorological data used (Sørensen et al., 2020), as well as the parametrization of the source term prior model (Tichý et al., 2020). To determine the overall posterior emission uncertainty, variants of log-normal models have been used recently (Dumont Le Brazidec et al., 2021; Liu et al., 2017). Here, we use a Gaussian model, due to its tractability and interpretability of posterior estimates.

Specifically, the uncertainty quantification of the estimated posterior

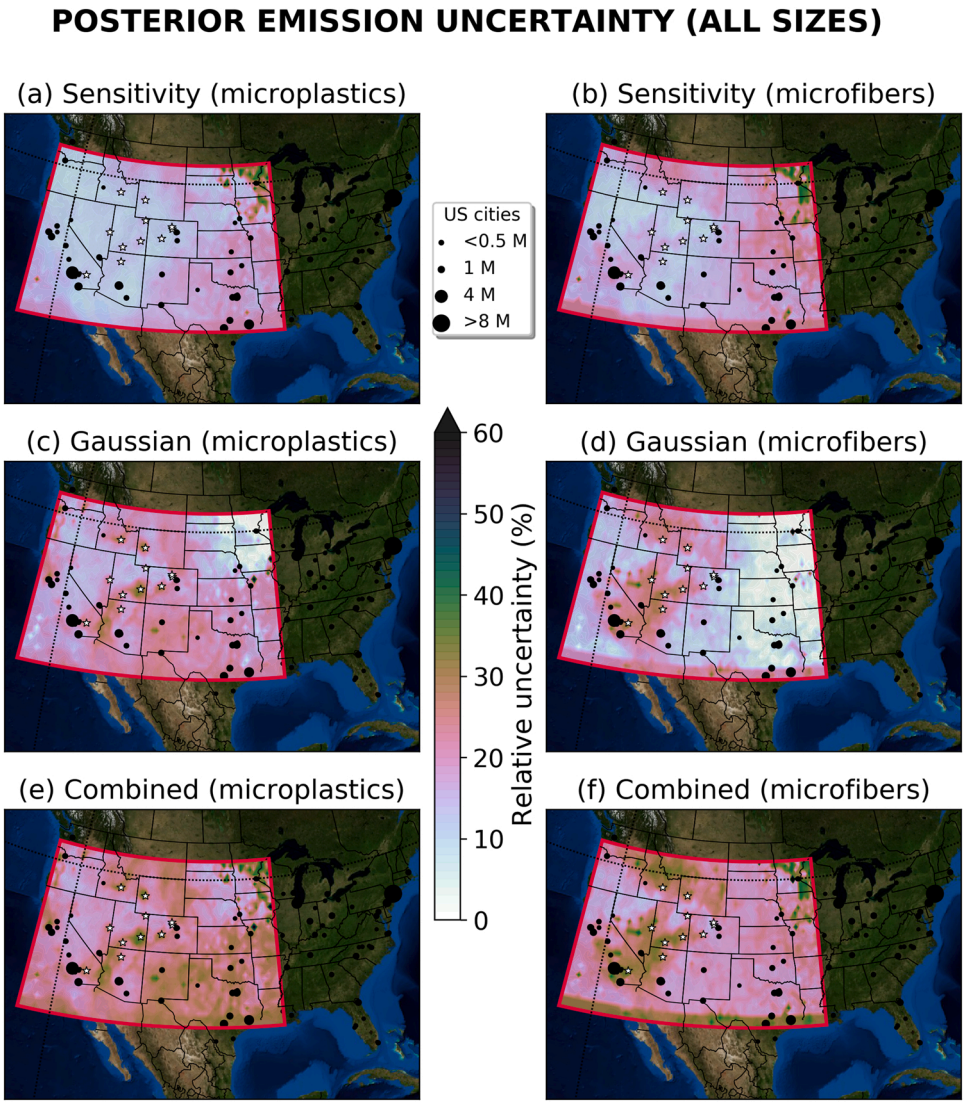

Fig. 6. Calculation of the posterior emission uncertainty of MPs and MFs (a, b) based on the sensitivity of the emissions to different scavenging coefficients, (c, d) using a Gaussian model (see Section 4.1), and (e, f) the propagated (combined) uncertainty.

emissions is based on the form of posterior distribution of the estimated emissions that is Gaussian with estimated mean value μ and covariance matrix Σ_x. Therefore, the uncertainty quantification of the estimated release rate is a direct output of the inversion method. Hence, we can calculate the uncertainty of each release element as:

$$x_i = \mu_{x,i} \pm \sqrt{\Sigma_{x,ii}} \quad (13)$$

where $\mu_{x,i}$ is ith element of the estimated mean value and $\Sigma_{x,ii}$ is ith diagonal element of the estimated covariance matrix, whose square root represents the standard deviation of the posterior emissions. To identify the total release uncertainty, we used properties of Gaussian distribution and calculated the uncertainty bounds of the posterior releases as follows:

$$U = \sum_i \mu_{x,i} \pm \sqrt{\Sigma_i \Sigma_{x,ii}} \quad (14)$$

The calculated posterior relative uncertainties for MPs and MFs are depicted in Fig. 6 for the first (ensemble) and the second (Gaussian) case, while the combined relative uncertainty is a propagation of the latter two. The uncertainty using the inversion algorithm ensemble of nine members shows that uncertainties grow up to 50% as we move to the eastern part of the inversion domain. In this part of the domain the SRMs were near zero (). The uncertainty quantification using Gaussian property of posterior distribution (Fig. 6c and d) depends on the estimated covariance matrix within the LS-APC model (Section 2.3) and is, in its essence, uncertainty of the posterior model caused by the sparsity of measurements rather than uncertainty of estimated emissions. The principle of the model is to tighten the values of the covariance matrix in spatial elements, where only few non-zero SRM are available (see on the eastern part). That subsequently tightens the estimated emissions to the prior value x_0 (see Eq. 6). However, this leaves low uncertainty in the posterior. On the other hand, in spatial elements with strong SRM, the estimated values of covariance matrix are so large that the estimated emissions do not depend on the prior value x_0, but rather on the data term. This causes larger variability in the covariance matrix resulting in larger uncertainty in Eq. (12).

Since the principles in uncertainty quantification in the case of ensemble approach and in the case of Gaussian approach are not consistent, we calculate a propagation of these two in Fig. 6e and f. We end up with uncertainties reaching 50% near the measurement stations and in the easternmost parts of the inversion domain.

4.2. Sensitivity to different source fractions

The extrapolation of the posterior emissions in global scale is based on the assumption of specific sources for MPs and MFs. While for MFs the main source is mostly clothing, this is not the case for MPS, as they are known to originate mainly from transportation (primary source), mineral dust (secondary source), agricultural activity (secondary source) and sea spray (secondary source), but perhaps from other sources not yet defined. The main question is what the exact fractions of these specific sources constitute total MPs. To tackle this lack of knowledge, we accepted that primary MPs (here road dust) contribute 15–31% (average 23%), as seen in the ocean (Boucher and Friot, 2017; Goßmann et al., 2021; Zhao et al., 2019) and we perturbed the rest of the sources building 30 ensemble members, each with different source contribution scenarios that can be seen in Table S2. We calculate the global emission uncertainty as the standard deviation of the global releases that resulted from this 30-member ensemble.

The absolute uncertainty is depicted in Fig. 3b, side-by-side with the global annual releases of MFs. Note that such an assessment is not possible for MFs, as we only assumed that they originated from clothing of the global population. Uncertainty reaches 80% where the largest oceanic emissions were calculated. This is a direct consequence of the fact that oceanic emissions calculated here are the vast majority of total emissions. Thus, any change is this source fraction () is crucial for the global emissions. A good example is Fig. 3c, which is a result of our calculated emission, but after applying source fractions from Brahney et al. (2021), as reported for deposition (see Table S2); the latter gives total emitted MPs to be four times lower (~2.4 Tg y^{-1}). Another problem with the oceanic emissions of MPs reported here is the restricted network of measurements (see also Section 3.2). Although an assessment of the introduced uncertainty over the inversion domain took place in the previous section, we admit that the deposition measurements used for inverse modelling in the present study are not unique to assess oceanic emissions. The reason is that they are located far from the US coast covering only a very small domain in the center of the inversion domain. On the other hand, oceanic surface area in the selected inversion domain lies in the west (Pacific Ocean) and in the south (Gulf of Mexico) covering only 10%. As expected, SRMs that are used in the inversion algorithm to define the connection between sources and observations are extremely low in oceanic regions (). A more careful assessment of the oceanic sources of MPs would require several observations to be taken in different oceanic locations, e.g., during ship campaigns and/or remote islands, which lacks in the current study.

Global uncertainty estimated for the land-based sources was much lesser, in the order of about 30% (Fig. 3b), as a result of the perturbation in the source fractions for agriculture, road and mineral dust. It follows the same pattern with emissions with maxima close to the largest sources.

4.3. Land – Ocean interactions

MPs and MFs emitted in the atmosphere, especially at smaller sizes, undergo long-range transport. Today, they have been already detected almost everywhere on earth (Allen et al., 2019, 2020; Bergmann et al., 2019; Dris et al., 2015, 2016; González-Pleiter et al., 2021b; Kelly et al., 2020; Qian and Ferro, 2008 and many others). However, it has been shown that oceanic emissions of MPs can be transported (Allen et al., 2020), similar to marine particles, when breaking waves cause bubbles of trapped air to rise to the surface and burst (Erinin et al., 2019). How much of the land-based emissions end into the ocean and vice versa remains unknown and is a frequent question by researchers conducting measurements often trying to interpret whether their measurements refer to primary or secondary sources.

To identify this, the reported modelled annual deposition of the emitted MPs caused by sea spray was masked towards land, whereas annual deposition from the land-based sources of agriculture, road and mineral dust was masked towards ocean, and the resulting budgets were calculated (Fig. 7). We report that 13 ± 6.5 kt y^{-1} of MPs were transferred from land to ocean or about 1.8% of the land emitted mass, due to the already mentioned limited transport due to the large particle sizes. The deposition occurred close to the shoreline, while a more consistent transport occurred at regions surrounded by land, such as the Mediterranean, North and Black Sea. Accordingly, about 122 ± 66.1 kt y^{-1} were transferred from ocean to land or about 1.4% of the oceanic emitted mass and mostly accumulated in mid-latitudes of the northern hemisphere (30–60°N), where the largest oceanic emissions were calculated (Fig. 3). The same latitudinal band of the southern hemisphere also gives high oceanic emissions, but land largely lacks there, except for the southernmost parts of South America and Australia. As regards to MFs, we estimate that 405 ± 201 kt are transported and deposited to the ocean annually.

Boucher and Friot (2017) reported that around 15% of marine plastics is a result of atmospheric transport and deposition to the global ocean. Between 5.3 and 14 Tg of plastics enter the global ocean annually (Eriksen et al., 2014; Jambeck et al., 2015; Jang et al., 2016). Although a rough estimation, combining these two numbers, it is found that 0.80–2.1 Tg y^{-1} is the number of plastics that are transported by air. Around 92% of these oceanic plastics are MPs (Auta et al., 2017; Eriksen et al., 2014), or 0.74–1.9 Tg y^{-1} (< 5 mm). Here, we report that 0.405

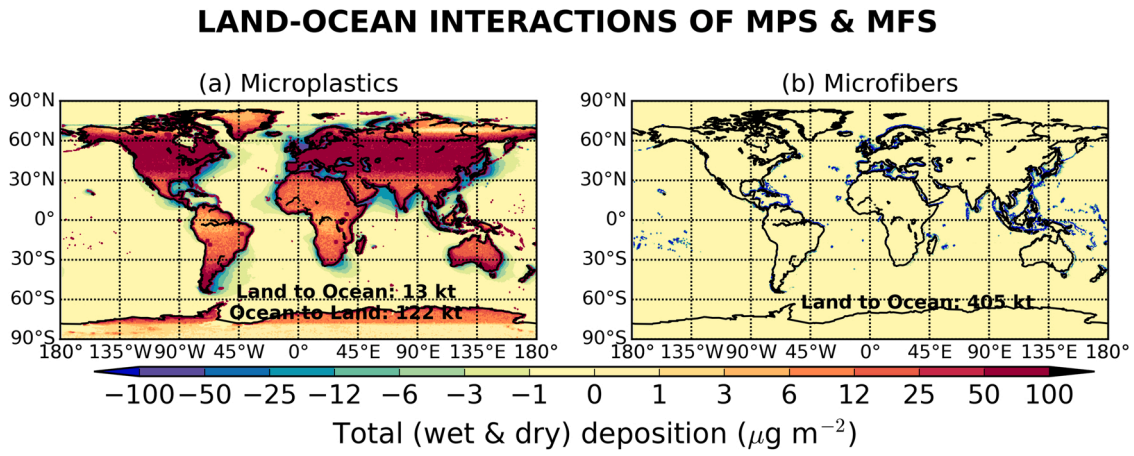

Fig. 7. (a) MPs emitted from the land that were deposited over the ocean annually and vice versa (ocean to land). (b) MFs emitted from global population that were deposited in the ocean.

$\pm$ 0.201 and 0.013 $\pm$ 0.0065 Tg y^{-1} of synthetic MFs (<2500 μm) and MPs (<250 μm), respectively, are transported from the land to ocean. This is comparable with the reported values although in the lowest range, albeit we have not considered larger sizes than 2500 μm for MFs and 250 μm for MPs that are heavier. Furthermore, atmospheric transport of MPs that end to the ocean are an order of magnitude lower than

Table 3
Observations of MPs and MFs in deposition and surface air samples from the global literature for various years. Considering that the modelled lifetime of MPs and MFs is very short, we assume that transport is less important; therefore, we use the global simulation for the year 2018 to assess how the modelled MPs and MFs compare with observations.

	Sampling method	Measured size	Location	Concentration	Year	This study
(Roblin et al., 2020)	Deposition	50 μm	Ireland	12 fibers m^{-2} d^{-1}	2017–2018	32 fibers m^{-2} d^{-1}
(Dris et al., 2016, 2015)	Deposition	50 μm	Paris	53–118 items m^{-2} d^{-1}	2014	200 items m^{-2} d^{-1}
(Trainic et al., 2020)	Outdoor active	5 μm	North Atlantic	0.01 items m^{-3}	2016	0.6 items m^{-3}
(Allen et al., 2019)	Deposition	5 μm	French Pyrenees	365 items m^{-2} d^{-1}	2017–2018	150 items m^{-2} d^{-1}
(Allen et al., 2020)	Outdoor active	5 μm	French Atlantic	2.9–9.6 items m^{-3}	2018	1.5 items m^{-3}
(Peñalver et al., 2021)	Outdoor active	10 μm	South Spain	36 ng m^{-3}	2017	48 ng m^{-3}
(Wright et al., 2020)	Deposition	5 μm	London	575–1008 items m^{-2} d^{-1}	2018	500 items m^{-2} d^{-1}
(Bergmann et al., 2019)	Snow deposition	11 μm	Arctic/Swiss Alps/Germany	1.4–66 items m^{-2} y^{-1}	2015–2017	180 items m^{-2} d^{-1}
(Materić et al., 2021)	Snow deposition	< 1 μm	Alps	42 kg km^{-2} y^{-1}	2017	NP not considered
(Abbasi et al., 2019)	Outdoor active	2 μm	Iran	0.3–1.1 items m^{-3}	2017	0.8 items m^{-3}
(Abbasi and Turner, 2021)	Deposition	< 100 μm	Iran	7–120 items m^{-2} d^{-1}	2019–2020	450 items m^{-2} d^{-1}
(Ding et al., 2021)	Outdoor active	< 200 μm	South China Sea	0.035 items m^{-3}	2019	0.5 items m^{-3}
(Klein and Fischer, 2019)	Deposition	5–13 μm	Hamburg	136–512 items m^{-2} d^{-1}	2017–2018	410 items m^{-2} d^{-1}
(Szewc et al., 2021)	Deposition	5 μm	Baltic Sea	136–512 items m^{-2} d^{-1}	2017–2018	115 items m^{-2} d^{-1}
(K.Liu et al., 2019a)	Outdoor active	< 1 mm	Shanghai, China	1.42 items m^{-3}	2018	1.5 items m^{-3}
(Cai et al., 2017)	Deposition	200–700 μm	Dongguan, China	175–313 items m^{-2} d^{-1}	2016	586 items m^{-2} d^{-1}
(Zhou et al., 2017)	Deposition	< 0.5 mm	Yantai, China	475 items m^{-2} d^{-1}	2016	489 items m^{-2} d^{-1}
(K.Liu et al., 2019b)	Outdoor active	20 μm	West Pacific coast	0.0–1.4 items m^{-3}	2019	0.7 items m^{-3}
(Knobloch et al., 2021)	Deposition	20 μm	New Zealand	1018 items m^{-2} d^{-1}	2020	549 items m^{-2} d^{-1}
(Huang et al., 2021)	Deposition	< 50 μm	Guangzhou, China	51–178 items m^{-2} d^{-1}	2018–2019	286 items m^{-2} d^{-1}
(Wang et al., 2020)	Outdoor active	60 μm	S. China Sea / E. Indian Ocean	0.04–0.08 items m^{-3}	2019	0.12–0.21 items m^{-3}
(Wang et al., 2021)	Outdoor active	20 μm	China Sea	0.0039 items m^{-3}	2020	0.45 items m^{-3}
(Liao et al., 2021)	Outdoor active	5 μm – 5 mm	Wenzhou, China	189 items m^{-3}	2019	0.74 items m^{-3}
(Tunahan Kaya et al., 2018)	Outdoor active	50 μm – 5 mm	Turkey	116–3424 items m^{-3}	2016–2017	0.19 items m^{-3}
(Asrin and Dipareza, 2019)	Outdoor active	500 μm – 5 mm	Indonesia	131–174 items m^{-3}	2017	1.5 items m^{-3}
(Li et al., 2020)	Outdoor active	5 μm – 2 mm	Beijing, China	5600–5700 items m^{-3}	2019	17 items m^{-3}
(Gaston et al., 2020)	Outdoor active	20–3000 μm	Cal State Univ., USA	13–22 items m^{-3}	2019	22 items m^{-3}
(Syafei et al., 2019)	Outdoor active	500–5000 μm	Indonesia	56–175 items m^{-3}	2018	1.8 items m^{-3}
(Akhbarizadeh et al., 2021)	Outdoor active	< 2.5	Iran	0.0–14 items m^{-3}	2016–2017	2.5 items m^{-3}
(González-Pleiter et al., 2021a)	Outdoor active	30–70 μm	Madrid, Spain	1.5–14 items m^{-3}	2020	2.9 items m^{-3}
(González-Pleiter et al., 2021b)	Deposition	2.3–12.6 mm	Collins Glacier, Antarctica	0.08–0.17 items m^{-2} d^{-1}	2020	1.5 items m^{-2} d^{-1}
(Truong et al., 2021)	Deposition	50–5000 μm	Ho Chi Minh, Vietnam	71–917 items m^{-2} d^{-1}	2018–2019	211 items m^{-2} d^{-1}
(Stanton et al., 2019)	Deposition	38 μm – 5 mm	Nottingham, UK	0–31 items m^{-2} d^{-1}	2018	188 items m^{-2} d^{-1}
(Hamilton et al., 2021)	Deposition	80–5000 μm	Nunavut, Canada	500–6000 items m^{-2} d^{-1}	2018	15 items m^{-2} d^{-1}
(Yukioka et al., 2020)	Deposition	75 μm – 5 mm	Kusatsu, Japan	0.4 items m^{-2} d^{-1}	2017	12 items m^{-2} d^{-1}
(Yukioka et al., 2020)	Deposition	75 μm – 5 mm	Da Nang, Vietnam	4.0 items m^{-2} d^{-1}	2017	8.6 items m^{-2} d^{-1}
(Yukioka et al., 2020)	Deposition	75 μm – 5 mm	Kathmandu, Nepal	12.5 items m^{-2} d^{-1}	2017	101 items m^{-2} d^{-1}
(Zhu et al., 2021)	Outdoor active	5–5000 μm	Beijing, China	393 items m^{-3}	2019	23 items m^{-3}
(Zhu et al., 2021)	Outdoor active	5–5000 μm	Tianjin, China	324 items m^{-3}	2019	14 items m^{-3}
(Zhu et al., 2021)	Outdoor active	5–5000 μm	Nanjing, China	177 items m^{-3}	2019	12 items m^{-3}
(Zhu et al., 2021)	Outdoor active	5–5000 μm	Sanghai, China	267 items m^{-3}	2019	20 items m^{-3}
(Zhu et al., 2021)	Outdoor active	5–5000 μm	Hangzhou, China	246 items m^{-3}	2019	13 items m^{-3}
(Allen et al., 2021)	Outdoor active	< 50 μm	Pic du Midi, France	0.09–0.66 items m^{-3}	2017	0.05 items m^{-3}

the riverine transported MPs to the ocean (3.3–14 Tg y^{-1}).

4.4. Independent validation and forecast of expected levels

As it was already mentioned in Section 3.1, the observations from Brahney et al. (2020) used in the inversion algorithm should not serve as measurements to validate the posterior emissions of MPs and MFs. The reason for this is because the inversion algorithm has been designed to reduce the model–observation mismatches. This means that the reduction of the posterior concentration mismatches with the observations is determined by the weighting that is given to the observations and, hence, such a comparison depends on this weighting (dependent observation). Therefore, the ideal comparison would be against measurements that were not included in the inversion algorithm. There are several literature records on MP and MF measurements in the environment using various techniques, both for surface concentrations and deposition rates (Table 3). They refer to the recent years between 2014 and 2020, whereas measured particles sizes are extremely large (up to 5000 μm) in most cases due to specific limitations of the available analytical techniques. In the present study, we report optimised MPs and MFs emissions for sizes up to 250 μm and 5000 μm, respectively. Our results suggest limited transport due to the large particle size considered. Therefore, we use MP and MF concentrations and deposition rates from Table 3 as a proxy to assess how modelled results from our global simulation for the year 2018 compare with observations assuming year-by-year meteorology has limited effect on transport of large particles.

We use the Gaussian kernel density estimation (KDE), which is a non-parametric way to estimate the probability density function (PDF) of a random variable (Parzen, 1962):

$$f(x) = \frac{1}{Nh}\sum_{i=1}^{N} K\left(\frac{x - x_i}{h}\right) \quad (15)$$

where K is the kernel, x_i the univariate independent and identically distributed point of the relationship between modelled and measured ammonia and h is a smoothing parameter called the bandwidth. KDE is a fundamental data smoothing tool that attempts to infer characteristics of a population, based on a finite dataset. It weighs the distance of all points in each specific location along the distribution. If there are more points grouped locally, the estimation is higher as the probability of seeing a point at that location increases. The kernel function is the specific mechanism used to weigh the points across the data set and it uses the bandwidth to limit the scope of the function. The latter is computed using the Scott's factor (Scott, 2015). We also provide the mean fractional bias (MFB) for modelled and measured separately for concentrations and deposition rates as follows:

$$MFB = \frac{1}{N}\frac{\sum_{i=1}^{N}(C_m - C_o)}{\sum_{i=1}^{N}\left(\frac{C_m + C_o}{2}\right)} \times 100\% \quad (16)$$

where C_m and C_o are the modelled and measured quantities and N is the total number of observations. MFB is a symmetric performance indicator that gives equal weights to under- or overestimated concentrations (minimum to maximum values range from −200% to 200%).

The comparison of modelled surface concentrations and deposition rates with the observations is shown in Fig. 8. As seen both in Fig. 8 and Table 3 the modelled concentrations are in the same order with observations except for some outliers (e.g., in Nunavut, Canada from Hamilton et al., 2021). The calculated MFBs suggest that the model tends to underestimate concentrations ($MFB_{con} = -57\%$) and overestimate deposition rates ($MFB_{dep} = +39\%$). The latter shows that more information is required to understand how efficient CCN or IN (Ganguly and Ariya, 2019b) MPs and MFs are, how dry deposition affects removal from the atmosphere and, in turn, how they should be modelled in global models. As regards to scavenging that is a more uncertain process,

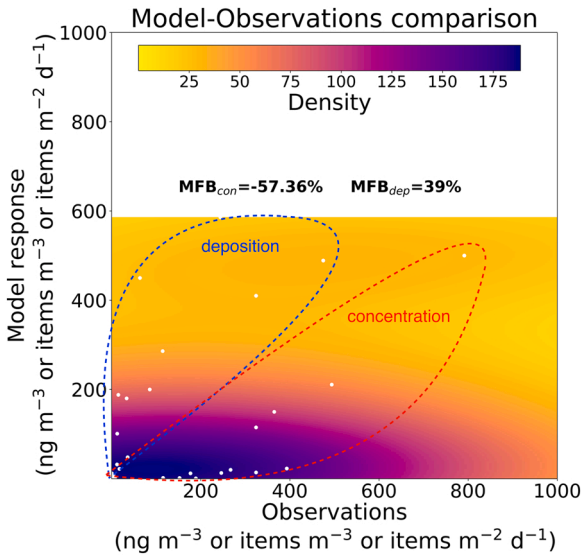

Fig. 8. Independent validation of modelled concentration and deposition of MPs and MFs against observations from the relevant literature (Table 3). Scatterplots of modelled results against observations were plotted using the Kernel density estimation, which is a way to estimate the probability density function (PDF) of a random variable in a non-parametric way. The Mean Fractional Bias (MFB) is also computed separately for concentrations and deposition rates.

we only assumed that MPs and MFs are scavenged moderately in and below clouds (Table S1), as they are synthetic polymers (macromolecules) and should have hydrophobic behavior. However, without specific measurements of the scavenging coefficients for MPs and MFs, it is impossible to know how they behave in the atmosphere, in order to accurately reproduce their transport and removal in global models. These properties are crucial for accurate representation of MPs, both in forward modelling (atmospheric dispersion of a known source), as well as in inverse algorithms (source quantification). Nevertheless, the simulations presented in this study can be used by researchers who plan to perform sampling and analysis of MPs and MFs in order to forecast the expected levels at any place on earth in high temporal and spatial resolutions (0.5°×0.5°, daily).

4.5. Robustness of the inverse modelling methodology

Brahney et al. (2021) have successfully managed to calculate total emissions of MPs, though presenting somewhat large model-observation mismatches. The core of their methodology was to minimize the cost function based on the goodness of fit between modelled values and measurements weighted by the model-observation error. Moreover, a scalar regularization term was added to suppress negative values of estimated emissions. Their estimated emissions are based on an optimized combination of five known annual sources, road dust, ocean, agricultural dust, population dust, and population. The combination is calculated using a global search method for these five sources with 30 possible strengths for each source (from zero to the value explaining the whole measurements). Since the estimated emissions rely on the usage of annual sources, the calculated emissions lack any temporal variation. This simplification imposes the shape of spatial distribution of emissions and might be the key reason for the poor fit of modelled values with measurements. In contrast with the aforementioned methodology, here we do not make use of any pre-computed source, but rather use a completely data-driven approach (Tichý et al., 2016) for the current spatial inversion domain (124–91°W, 29–47°N). This method calculates MP and MF emissions with large spatiotemporal resolution (0.5°×0.5°, daily).

5. Conclusions

We have used a robust Bayesian inverse modelling algorithm combined with a Lagrangian particle dispersion model suitable to track deposited particles in backward mode to calculate high spatiotemporal emissions of MPs and MFs from observations in the Western USA. We further extrapolate these calculations to retrieve global estimates of atmospheric MP and MF fluxes from different sectorial emissions. Finally, we feed the calculated emissions into a dispersion model to track global atmospheric dynamics and budgets of MPs and MFs. Our results are openly accessible and can be used as a proxy from research groups conducting surface concentration and deposition measurements to know the expected levels of MPs and MFs at any given place on earth. Further conclusions are summarised below:

- Around 9.0 ± 3.8 kt y^{-1} of atmospheric MPs of size up to 250 μm and 244 ± 129 kt y^{-1} of MFs of size up to 2500 μm were released in the inversion domain that includes central and west USA. Lower emissions closer to the observations are due to remoteness of the stations (far from any man-made activity).
- Global MP emissions were estimated to be 9.6 ± 3.6 Tg y^{-1}, whereas MF emissions equal to 6.5 ± 2.9 Tg y^{-1}.
- Ocean dominates MP emissions with 8.9 ± 3.5 Tg y^{-1}, as insoluble plastics accumulate at the surface of the ocean with time and are resuspended similar to sea spray aerosols. We note that this calculation is highly uncertain because (i) the inversion domain covers a small oceanic surface that can be used in interpolation, (ii) the deposition measurements used in the inversion are far from the ocean, thus inappropriate to constrain oceanic emissions, and (iii) it is assumed that a constant number of oceanic microplastics is released globally following sea spray.
- Agricultural activities resuspend around 0.31 ± 0.13 Tg y^{-1}, road dust contributes another 0.28 ± 0.12 Tg y^{-1}, and mineral dust 0.10 ± 0.052 Tg y^{-1}.
- The largest emissions are calculated for Asia (MPs: 250 ± 120 kt y^{-1} – MFs: 3700 ± 1300 kt y^{-1}), North America (MPs: 130 ± 55.4 kt y^{-1} – MFs: 280 ± 120 kt y^{-1}), Africa (MPs: 110 ± 55.1 kt y^{-1} – MFs: 970 ± 452 kt y^{-1}) and Europe (MPs: 88 ± 42 kt y^{-1} – MFs: 460 ± 140 kt y^{-1}), while the rest of the continents have smaller shares in annual emissions.
- Global average monthly mass concentrations were at maximum 47 ng m^{-3} for MPs and 33 ng m^{-3} for MFs at the surface, while both are rapidly removed from the atmosphere, due to the small lifetimes affected by their large particle sizes.
- The largest deposition from agricultural sources (annual total: 310 ± 155 kt y^{-1}) occurred in Central USA, in the Indo-Gangetic Plain and the North China Plain, all regions of great agricultural activity. Road MPs (annual total: 279 ± 145 kt y^{-1}) were mostly deposited in the US East Coast, Central Europe, and Southeastern Asia, whereas mineral dust MPs deposited near Sahara and Middle East (annual total: 100 ± 53 kt y^{-1}). Oceanic MPs were deposited mostly in the Ocean.
- Only 1.8% of the land MP mass emissions (13 ± 6.6 kt y^{-1}) were transferred to ocean, due to the limited transport of large particle considered. About 1.4% (122 ± 65 kt y^{-1}) were transferred from ocean to land and accumulated in mid-latitudes of the north hemisphere.
- It is reported that 0.74–1.9 Tg y^{-1} of MPs (< 5 mm) are globally transported by air from land to ocean. We calculate that 0.418 ± 0.201 of synthetic MFs (<2500 μm) and MPs (<250 μm), are transported from the land to ocean. This close to the reported values although in the lowest range, due to exclusion of larger sizes (> 2500 μm for MFs and >250 μm for MPs) from this study that are heavier. Atmospheric transport of MPs that end to the ocean are an order of magnitude lower than the riverine transported MPs to the ocean (3.3–14 Tg y^{-1})
- The largest continental MP deposition occurred in Asia (267 ± 121 kt y^{-1}), North America (160 ± 71 kt y^{-1}), Africa (114 ± 59 kt y^{-1}) and Europe (102 ± 45 kt y^{-1}) similar to MFs (Asia: 3792 ± 1933 kt y^{-1}, America: 846 ± 209 kt y^{-1}, Africa: 801 ± 372 kt y^{-1}, Europe: 598 ± 253 kt y^{-1}).
- The largest oceanic MP deposition occurred in the Atlantic (1718 ± 899.5 kt y^{-1}), Pacific (2751 ± 1225 kt y^{-1}), Indian (1435 ± 766 kt y^{-1}) and Southern Ocean (2289 ± 1185 kt y^{-1}).

Since the particles considered in the present study are large and their atmospheric lifetimes short, we validated the present results with global measurement taken during the last decade assuming that meteorology does not have a major effect on particles that are removed from the atmosphere very fast. We report that the current model set-up underestimates surface concentrations and overestimates deposition rates. This means that the coefficients for in-cloud and below-cloud scavenging and dry deposition processes that are considered in global models need to be updated.

CRediT authorship contribution statement

Nikolaos Evangeliou: Conceptualization, Lagrangian modelling, Investigation, Writing – review & editing, Supervision. **Ondřej Tichý:** Methodology, Inverse modelling algorithm development & optimisation, Writing – review & editing. **Sabine Eckhardt:** Lagrangian modelling, Writing – review & editing. **Christine Groot Zwaaftink:** Calculation of global dust emissions using FLEXDUST model, Writing – review & editing. **Janice Brahney:** Sample collection & analysis, Review & editing.

Declaration of Competing Interest

The authors declare that they have no competing financial interests or personal relationships that could have influenced the work reported in this paper.

Acknowledgements

The work was funded by NILU and COMBAT (Quantification of Global Ammonia Sources constrained by a Bayesian Inversion Technique) project funded by ROMFORSK – Program for romforskning of the Research Council of Norway (Project ID: 275407), website: https://prosjektbanken.forskningsradet.no/project/FORISS/275407?Kilde=FORISS&distribution=Ar&chart=bar&calcType=funding&Sprak=no&sortBy=date&sortOrder=desc&resultCount= 30&offset= 0&ProgAkt.3 =ROMFORSK-Program+for+romforskning. Dr. Ondřej Tichý was supported by the Czech Science Foundation, grant no. GA20-27939S.

Novelty

We combine high-quality deposition measurements from the Western USA with a dispersion model and an inverse modelling algorithm to constrain global atmospheric emissions of microplastics (MPs) and microfibers (MFs) in high spatiotemporal resolution. The only global dispersion model that can track deposition backward in time is used for the first time in an inverse modelling approach. The constrained emissions are used further to model global atmospheric dynamics of MPs and MFs. We address the expected surface concentrations, and deposition rates of atmospheric MPs and MFs in a gridded product that aims at assisting researchers conducting measurements at a global scale.

Appendix A. Supporting information

Supplementary data associated with this article can be found in the online version at doi:10.1016/j.jhazmat.2022.128585.

References

Abbasi, S., Keshavarzi, B., Moore, F., Turner, A., Kelly, F.J., Dominguez, A.O., Jaafarzadeh, N., 2019. Distribution and potential health impacts of microplastics and microrubbers in air and street dusts from Asaluyeh County, Iran. Environ. Pollut. 244, 153–164. https://doi.org/10.1016/j.envpol.2018.10.039.

Abbasi, S., Turner, A., 2021. Dry and wet deposition of microplastics in a semi-arid region (Shiraz, Iran). Sci. Total Environ. 786, 147358 https://doi.org/10.1016/j.scitotenv.2021.147358.

Akhbarizadeh, R., Dobaradaran, S., Amouei Torkmahalleh, M., Saeedi, R., Aibaghi, R., Faraji Ghasemi, F., 2021. Suspended fine particulate matter (PM2.5), microplastics (MPs), and polycyclic aromatic hydrocarbons (PAHs) in air: Their possible relationships and health implications. Environ. Res. 192, 110339 https://doi.org/10.1016/j.envres.2020.110339.

Allen, S., Allen, D., Baladima, F., Phoenix1, V.R., Thomas, J.L., Roux, G., Le, Sonke, J.E., 2021. Evidence of free tropospheric and long-range Observatory. Nat. Commun. 12, 7242. https://doi.org/10.1038/s41467-021-27454-7.

Allen, S., Allen, D., Moss, K., Le Roux, G., Phoenix, V.R., Sonke, J.E., 2020. Examination of the ocean as a source for atmospheric microplastics. PLoS One 15, 1–14. https://doi.org/10.1371/journal.pone.0232746.

Allen, S., Allen, D., Phoenix, V.R., Le Roux, G., Durántez Jiménez, P., Simonneau, A., Binet, S., Galop, D., 2019. Atmospheric transport and deposition of microplastics in a remote mountain catchment. Nat. Geosci. 12, 339–344. https://doi.org/10.1038/s41561-019-0335-5.

An, L., Liu, Q., Deng, Y., Wu, W., Gao, Y., Ling, W., 2020. Sources of microplastic in the environment. Handbook of Environmental Chemistry. Springer, pp. 143–159. https://doi.org/10.1007/698_2020_449.

Asrin, N., Dipareza, A., 2019. Microplastics in ambient air (case study: Urip Sumoharjo Street and Mayjend Sungkono Street of Surabaya City, Indonesia). IAETSD J. Adv. Res. Appl. Sci. 6, 54–57.

Athey, S.N., Adams, J.K., Erdle, L.M., Jantunen, L.M., Helm, P.A., Finkelstein, S.A., Diamond, M.L., 2020. The widespread environmental footprint of indigo denim microfibers from blue jeans. Environ. Sci. Technol. Lett. 7, 840–847. https://doi.org/10.1021/acs.estlett.0c00498.

Auta, H.S., Emenike, C.U., Fauziah, S.H., 2017. Distribution and importance of microplastics in the marine environmentA review of the sources, fate, effects, and potential solutions. Environ. Int. 102, 165–176. https://doi.org/10.1016/j.envint.2017.02.013.

Barnes, D.K.A., Galgani, F., Thompson, R.C., Barlaz, M., 2009. Accumulation and fragmentation of plastic debris in global environments. Philos. Trans. R. Soc. B Biol. Sci. 364, 1985–1998. https://doi.org/10.1098/rstb.2008.0205.

Bergmann, M., Mützel, S., Primpke, S., Tekman, M.B., Trachsel, J., Gerdts, G., 2019. White and wonderful? Microplastics prevail in snow from the Alps to the Arctic. Sci. Adv. 5, 1–11. https://doi.org/10.1126/sciadv.aax1157.

Blettler, M.C.M., Abrial, E., Khan, F.R., Sivri, N., Espinola, L.A., 2018. Freshwater plastic pollution: Recognizing research biases and identifying knowledge gaps. Water Res. 143, 416–424. https://doi.org/10.1016/j.watres.2018.06.015.

Bond, T.C., Doherty, S.J., Fahey, D.W., Forster, P.M., Berntsen, T., Deangelo, B.J., Flanner, M.G., Ghan, S., Kärcher, B., Koch, D., Kinne, S., Kondo, Y., Quinn, P.K., Sarofim, M.C., Schultz, M.G., Schulz, M., Venkataraman, C., Zhang, H., Zhang, S., Bellouin, N., Guttikunda, S.K., Hopke, P.K., Jacobson, M.Z., Kaiser, J.W., Klimont, Z., Lohmann, U., Schwarz, J.P., Shindell, D., Storelvmo, T., Warren, S.G., Zender, C.S., 2013. Bounding the role of black carbon in the climate system: A scientific assessment. J. Geophys. Res. Atmos. 118, 5380–5552. https://doi.org/10.1002/jgrd.50171.

Boucher, J., Friot, D., 2017. Primary Microplastics in the Oceans: a Global Evaluation of Sources, Primary microplastics in the oceans: A global evaluation of sources. IUCN Gland, Switzerland. https://doi.org/10.2305/iucn.ch.2017.01.en.

Brahney, J., Hallerud, M., Heim, E., Hahnenberger, M., Sukumaran, S., 2020. Plastic rain in protected areas of the United States. Science 368, 1257–1260. https://doi.org/10.1126/science.aaz5819.

Brahney, J., Mahowald, N., Prank, M., Cornwell, G., Klimont, Z., Matsui, H., Prather, K.A., 2021. Constraining the atmospheric limb of the plastic cycle. Proc. Natl. Acad. Sci. U.S.A. 118, e2020719118 https://doi.org/10.1073/pnas.2020719118.

Browne, M.A., Crump, P., Niven, S.J., Teuten, E., Tonkin, A., Galloway, T., Thompson, R., 2011. Accumulation of microplastic on shorelines woldwide: sources and sinks. Environ. Sci. Technol. 45, 9175–9179. https://doi.org/10.1021/es201811s.

Cai, L., Wang, J., Peng, J., Tan, Z., Zhan, Z., Tan, X., Chen, Q., 2017. Characteristic of microplastics in the atmospheric fallout from Dongguan city, China: preliminary research and first evidence. Environ. Sci. Pollut. Res. 24, 24928–24935. https://doi.org/10.1007/s11356-017-0116-x.

Carpenter, E.J., Anderson, S.J., Harvey, G.R., Miklas, H.P., Peck, B.B., 1972. Polystyrene spherules in coastal waters. Science 178, 749–750. https://doi.org/10.1126/science.178.4062.749.

Carpenter, E.J., Smith, K.L., 1972. Plastics on the Sargasso sea surface. Science 175, 1240–1241. https://doi.org/10.1126/science.175.4027.1240.

Cassiani, M., Stohl, A., Brioude, J., 2014. Lagrangian stochastic modelling of dispersion in the convective boundary layer with skewed turbulence conditions and a vertical density gradient: formulation and implementation in the FLEXPART model. Bound.-Layer. Meteor. 154, 367–390. https://doi.org/10.1007/s10546-014-9976-5.

Chae, Y., An, Y.J., 2018. Current research trends on plastic pollution and ecological impacts on the soil ecosystem: a review. Environ. Pollut. 240, 387–395. https://doi.org/10.1016/j.envpol.2018.05.008.

Chen, G., Feng, Q., Wang, J., 2020. Mini-review of microplastics in the atmosphere and their risks to humans. Sci. Total Environ. 703, 135504 https://doi.org/10.1016/j.scitotenv.2019.135504.

Colton, J.B., Knapp, F.D., Bums, B.R., 1974. Plastic particles in surface waters of the Northwestern Atlantic. Science 185, 491–497.

Coyle, R., Hardiman, G., Driscoll, K.O., 2020. Microplastics in the marine environment: a review of their sources, distribution processes, uptake and exchange in ecosystems. Case Stud. Chem. Environ. Eng. 2, 100010 https://doi.org/10.1016/j.cscee.2020.100010.

De Meutter, P., Hoffman, I., Ungar, K., 2020. On the model uncertainties in Bayesian source reconstruction using the emission inverse modelling system FREARtool v1.0 and the Lagrangian transport and dispersion model Flexpart v9.0.2. Geosci. Model Dev. Discuss. 1–23. https://doi.org/10.5194/gmd-2020-162.

Ding, Y., Zou, X., Wang, C., Feng, Z., Wang, Y., Fan, Q., Chen, H., 2021. The abundance and characteristics of atmospheric microplastic deposition in the northwestern South China Sea in the fall. Atmos. Environ. 253, 118389 https://doi.org/10.1016/j.atmosenv.2021.118389.

Dris, R., Gasperi, J., Rocher, V., Saad, M., Renault, N., Tassin, B., 2015. Microplastic contamination in an urban area: a case study in Greater Paris. Environ. Chem. 12, 592–599. https://doi.org/10.1071/EN14167.

Dris, R., Gasperi, J., Saad, M., Mirande, C., Tassin, B., 2016. Synthetic fibers in atmospheric fallout: a source of microplastics in the environment? Mar. Pollut. Bull. 104, 290–293. https://doi.org/10.1016/j.marpolbul.2016.01.006.

Dumont Le Brazidec, J., Bocquet, M., Saunier, O., Roustan, Y., 2021. Quantification of the modelling uncertainties in atmospheric release source assessment and application to the reconstruction of the autumn 2017 Ruthenium 106 source. Atmos. Chem. Phys. Discuss. 1–28. https://doi.org/10.5194/acp-2020-1129.

Eckhardt, S., Cassiani, M., Evangeliou, N., Sollum, E., Pisso, I., Stohl, A., 2017. Source-receptor matrix calculation for deposited mass with the Lagrangian particle dispersion model FLEXPART v10.2 in backward mode. Geosci. Model Dev. 10 https://doi.org/10.5194/gmd-10-4605-2017.

Eriksen, M., Lebreton, L.C.M., Carson, H.S., Thiel, M., Moore, C.J., Borerro, J.C., Galgani, F., Ryan, P.G., Reisser, J., 2014. Plastic pollution in the world's oceans: more than 5 trillion plastic pieces weighing over 250,000 tons afloat at sea. PLoS One 9, 1–15. https://doi.org/10.1371/journal.pone.0111913.

Erinin, M.A., Wang, S.D., Liu, R., Towle, D., Liu, X., Duncan, J.H., 2019. Spray generation by a plunging breaker. Geophys. Res. Lett. 46, 8244–8251. https://doi.org/10.1029/2019GL082831.

Evangeliou, N., Balkanski, Y., Eckhardt, S., Cozic, A., Van Damme, M., Coheur, P.-F., Clarisse, L., Shephard, M., Cady-Pereira, K., Hauglustaine, D., 2021. 10–year satellite–constrained fluxes of ammonia improve performance of chemistry transport models. Atmos. Chem. Phys. 21, 4431–4451. https://doi.org/10.5194/acp-21-4431-2021.

Evangeliou, N., Grythe, H., Klimont, Z., Heyes, C., Eckhardt, S., Lopez-Aparicio, S., Stohl, A., 2020. Atmospheric transport is a major pathway of microplastics to remote regions. Nat. Commun. 11. https://doi.org/10.1038/s41467-020-17201-9.

Fakour, H., Lo, S.L., Yoashi, N.T., Massao, A.M., Lema, N.N., Mkhontfo, F.B., Jomalema, P.C., Jumanne, N.S., Mbuya, B.H., Mtweve, J.T., Imani, M., 2021. Quantification and analysis of microplastics in farmland soils: characterization, sources, and pathways. Agriculture 11. https://doi.org/10.3390/agriculture11040330.

Fendall, L.S., Sewell, M.A., 2009. Contributing to marine pollution by washing your face: Microplastics in facial cleansers. Mar. Pollut. Bull. 58, 1225–1228. https://doi.org/10.1016/j.marpolbul.2009.04.025.

Forster, C., Stohl, A., Seibert, P., 2007. Parameterization of convective transport in a Lagrangian particle dispersion model and its evaluation. J. Appl. Meteorol. Clim. 46, 403–422. https://doi.org/10.1175/JAM2470.1.

Ganesan, A.L., Rigby, M., Zammit-Mangion, A., Manning, A.J., Prinn, R.G., Fraser, P.J., Harth, C.M., Kim, K.R., Krummel, P.B., Li, S., Mühle, J., O'Doherty, S.J., Park, S., Salameh, P.K., Steele, L.P., Weiss, R.F., 2014. Characterization of uncertainties in atmospheric trace gas inversions using hierarchical Bayesian methods. Atmos. Chem. Phys. 14, 3855–3864. https://doi.org/10.5194/acp-14-3855-2014.

Ganguly, M., Ariya, P.A., 2019a. Ice nucleation of model nanoplastics and microplastics: a novel synthetic protocol and the influence of particle capping at diverse atmospheric environments. ACS Earth Space Chem. 3, 1729–1739. https://doi.org/10.1021/acsearthspacechem.9b00132.

Ganguly, M., Ariya, P.A., 2019b. Ice nucleation of model nanoplastics and microplastics: a novel synthetic protocol and the influence of particle capping at diverse atmospheric environments. ACS Earth Space Chem. 3, 1729–1739. https://doi.org/10.1021/acsearthspacechem.9b00132.

Gao, J., 2017. Downscaling Global Spatial Population Projections from 1/8-degree to 1-km Grid Cells. NCAR Tech. Note 9.

Gaston, E., Woo, M., Steele, C., Sukumaran, S., Anderson, S., 2020. Microplastics differ between indoor and outdoor air masses: insights from multiple microscopy methodologies. Appl. Spectrosc. https://doi.org/10.1177/0003702820920652.

Gavigan, J., Kefela, T., Macadam-Somer, I., Suh, S., Geyer, R., 2020. Synthetic microfiber emissions to land rival those to waterbodies and are growing. PLoS One 15, 1–13. https://doi.org/10.1371/journal.pone.0237839.

Gewert, B., Plassmann, M.M., Macleod, M., 2015. Pathways for degradation of plastic polymers floating in the marine environment. Environ. Sci. Process. Impacts 17, 1513–1521. https://doi.org/10.1039/c5em00207a.

Godfrey, M., 2021. Toward eliminating pre-consumer emissions of microplastics from the textile industry. San Francisco.

Golub, G.H., Hansen, P.C., O'Leary, D.P., 1999. Tikhonov regularization and total least squares. SIAM J. Matrix Anal. Appl. 21, 185–194. https://doi.org/10.1137/S0895479897326432.

González-Pleiter, M., Edo, C., Aguilera, Á., Viúdez-Moreiras, D., Pulido-Reyes, G., González-Toril, E., Osuna, S., de Diego-Castilla, G., Leganés, F., Fernández-Piñas, F., Rosal, R., 2021a. Occurrence and transport of microplastics sampled within and

above the planetary boundary layer. Sci. Total Environ. 761, 143213 https://doi.org/10.1016/j.scitotenv.2020.143213.
González-Pleiter, M., Edo, C., Velázquez, D., Casero-Chamorro, M.C., Leganés, F., Quesada, A., Fernández-Piñas, F., Rosal, R., 2020. First detection of microplastics in the freshwater of an Antarctic specially protected area. Mar. Pollut. Bull. 161, 1–6. https://doi.org/10.1016/j.marpolbul.2020.111811.
González-Pleiter, M., Lacerot, G., Edo, C., Pablo Lozoya, J., Leganés, F., Fernández-Pina&tild;s, F., Rosal, R., Teixeira-De-Mello, F., 2021b. A pilot study about microplastics and mesoplastics in an Antarctic glacier. Cryosphere 15, 2531–2539. https://doi.org/10.5194/tc-15-2531-2021.
Goßmann, I., Halbach, M., Scholz-Böttcher, B.M., 2021. Car and truck tire wear particles in complex environmental samples – a quantitative comparison with "traditional" microplastic polymer mass loads. Sci. Total Environ. 773, 145667 https://doi.org/10.1016/j.scitotenv.2021.145667.
Gouin, T., 2021. Addressing the importance of microplastic particles as vectors for long-range transport of chemical contaminants: perspective in relation to prioritizing research and regulatory actions. Micro Nanoplastics 1, 1–19. https://doi.org/10.1186/s43591-021-00016-w.
Gregory, M.R., 1996. Plastic scrubbers in hand cleansers: a further (and minor) source for marine pollution identified. Mar. Pollut. Bull. 32, 867–871. https://doi.org/10.1016/S0025-326X(96)00047-1.
Grigoratos, T., Martini, G., 2015. Brake wear particle emissions: a review. Environ. Sci. Pollut. Res. 22, 2491–2504. https://doi.org/10.1007/s11356-014-3696-8.
Grigoratos, T., Martini, G., 2014. Non-exhaust traffic related emissions. Brake and tyre wear PM. Publications Office of the European Union. Luxembourg. https://doi.org/10.2790/21481.
Groot Zwaaftink, C.D., Arnalds, Ó., Dagsson-Waldhauserova, P., Eckhardt, S., Prospero, J.M., Stohl, A., 2017. Temporal and spatial variability of Icelandic dust emissions and atmospheric transport. Atmos. Chem. Phys. 17, 10865–10878. https://doi.org/10.5194/acp-17-10865-2017.
Grythe, H., Kristiansen, N.I., Groot Zwaaftink, C.D., Eckhardt, S., Ström, J., Tunved, P., Krejci, R., Stohl, A., 2017. A new aerosol wet removal scheme for the Lagrangian particle model FLEXPARTv10. Geosci. Model Dev. 10, 1447–1466. https://doi.org/10.5194/gmd-10-1447-2017.
Grythe, H., Ström, J., Krejci, R., Quinn, P., Stohl, A., 2014. A review of sea-spray aerosol source functions using a large global set of sea salt aerosol concentration measurements. Atmos. Chem. Phys. 14, 1277–1297. https://doi.org/10.5194/acp-14-1277-2014.
Habib, R.Z., Thiemann, T., Al Kendi, R., 2020. Microplastics and wastewater treatment plants—a review. J. Water Resour. Prot. 12, 1–35. https://doi.org/10.4236/jwarp.2020.121001.
Halle, L.L., Palmqvist, A., Kampmann, K., Khan, F.R., 2020. Ecotoxicology of micronized tire rubber: past, present and future considerations. Sci. Total Environ. 706, 135694 https://doi.org/10.1016/j.scitotenv.2019.135694.
Hamilton, B.M., Bourdages, M.P.T., Geoffroy, C., Vermaire, J.C., Mallory, M.L., Rochman, C.M., Provencher, J.F., 2021. Microplastics around an Arctic seabird colony: particle community composition varies across environmental matrices. Sci. Total Environ. 773, 145536 https://doi.org/10.1016/j.scitotenv.2021.145536.
Hansen, P.C., O'Leary, D.P., 1993. The use of the L-curve in the regularization of discrete ill-posed problems. Siam J. Sci. Comput. 1487–1503.
Harne, R., 2019. Studies on plastic bezoar ingestion in free range axis deer in summer. J. Anim. Res. 383–386. https://doi.org/10.30954/2277-940x.02.2019.25.
Hartmann, N.B., Hüffer, T., Thompson, R.C., Hassellöv, M., Verschoor, A., Daugaard, A. E., Rist, S., Karlsson, T., Brennholt, N., Cole, M., Herrling, M.P., Hess, M.C., Ivleva, N. P., Lusher, A.L., Wagner, M., 2019. Are we speaking the same language? Recommendations for a definition and categorization framework for plastic debris. Environ. Sci. Technol. 53, 1039–1047. https://doi.org/10.1021/acs.est.8b05297.
Hegg, D.A., Warren, S.G., Grenfell, T.C., Doherty, S.J., Larson, T.V., Clarke, A.D., 2009. Source attribution of black carbon in arctic snow. Environ. Sci. Technol. 43, 4016–4021. https://doi.org/10.1021/es803623f.
Henry, B., Laitala, K., Klepp, I.G., 2019. Microfibres from apparel and home textiles: prospects for including microplastics in environmental sustainability assessment. Sci. Total Environ. 652, 483–494. https://doi.org/10.1016/j.scitotenv.2018.10.166.
Höök, M., Tang, X., 2013. Depletion of fossil fuels and anthropogenic climate change-a review. Energy Policy 52, 797–809. https://doi.org/10.1016/j.enpol.2012.10.046.
Huang, Y., He, T., Yan, M., Yang, L., Gong, H., Wang, W., Qing, X., Wang, J., 2021. Atmospheric transport and deposition of microplastics in a subtropical urban environment. J. Hazard. Mater. 416, 126168 https://doi.org/10.1016/j.jhazmat.2021.126168.
Jambeck, J., Geyer, R., Wilcox, C., Siegler, T.R., Perryman, M., Andrady, A., Narayan, R., Law, K.L., 2015. Plastic waste inputs from land into the ocean 347. https://doi.org/10.1126/science.1260352.
Jan Kole, P., Löhr, A.J., Van Belleghem, F.G.A.J., Ragas, A.M.J., 2017a. Wear and tear of tyres: a stealthy source of microplastics in the environment. Int. J. Environ. Res. Public Health 14. https://doi.org/10.3390/ijerph14101265.
Jan Kole, P., Löhr, A.J., Van Belleghem, F.G.A.J., Ragas, A.M.J., 2017b. Wear and tear of tyres: a stealthy source of microplastics in the environment. Int. J. Environ. Res. Public Health 14, 1–4. https://doi.org/10.3390/ijerph14101265.
Jang, M., Shim, W.J., Han, G.M., Rani, M., Song, Y.K., Hong, S.H., 2016. Styrofoam Debris as a Source of Hazardous Additives for Marine Organisms. Environ. Sci. Technol. 50, 4951–4960. https://doi.org/10.1021/acs.est.5b05485.
Jones, B., O'Neill, B.C., 2016. Spatially explicit global population scenarios consistent with the shared socioeconomic pathways. Environ. Res. Lett. 11. https://doi.org/10.1088/1748-9326/11/8/084003.
Kelly, A., Lannuzel, D., Rodemann, T., Meiners, K.M., Auman, H.J., 2020. Microplastic contamination in east Antarctic sea ice. Mar. Pollut. Bull. 154, 111130 https://doi.org/10.1016/j.marpolbul.2020.111130.
Klein, M., Fischer, E.K., 2019. Microplastic abundance in atmospheric deposition within the Metropolitan area of Hamburg, Germany. Sci. Total Environ. 685, 96–103. https://doi.org/10.1016/j.scitotenv.2019.05.405.
Knobloch, E., Ruffell, H., Aves, A., Pantos, O., Gaw, S., Revell, L.E., 2021. Comparison of Deposition Sampling Methods to Collect Airborne Microplastics in Christchurch, New Zealand. Water Air Soil Pollut. 232. https://doi.org/10.1007/s11270-021-05080-9.
Kullback, S., Leibler, R.A., 1951. On information and sufficiency. Ann. Math. Stat. 22, 79–86. https://doi.org/10.1214/aoms/1177729694.
Lebreton, L., Egger, M., Slat, B., 2019. A global mass budget for positively buoyant macroplastic debris in the ocean. Sci. Rep. 9, 1–10. https://doi.org/10.1038/s41598-019-49413-5.
Lehner, R., Weder, C., Petri-Fink, A., Rothen-Rutishauser, B., 2019. Emergence of nanoplastic in the environment and possible impact on human health. Environ. Sci. Technol. 53, 1748–1765. https://doi.org/10.1021/acs.est.8b05512.
Li, Y., Shao, L., Wang, W., Zhang, M., Feng, X., Li, W., Zhang, D., 2020. Airborne fiber particles: types, size and concentration observed in Beijing. Sci. Total Environ. 705, 135967 https://doi.org/10.1016/j.scitotenv.2019.135967.
Liao, Z., Ji, X., Ma, Y., Lv, B., Huang, W., Zhu, X., Fang, M., Wang, Q., Wang, X., Dahlgren, R., Shang, X., 2021. Airborne microplastics in indoor and outdoor environments of a coastal city in Eastern China. J. Hazard. Mater. 417, 126007 https://doi.org/10.1016/j.jhazmat.2021.126007.
Liu, J., Yang, Y., Ding, J., Zhu, B., Gao, W., 2019. Microfibers: a preliminary discussion on their definition and sources. Environ. Sci. Pollut. Res. 26, 29497–29501. https://doi.org/10.1007/s11356-019-06265-w.
Liu, K., Wang, X., Fang, T., Xu, P., Zhu, L., Li, D., 2019a. Source and potential risk assessment of suspended atmospheric microplastics in Shanghai. Sci. Total Environ. 675, 462–471. https://doi.org/10.1016/j.scitotenv.2019.04.110.
Liu, K., Wu, T., Wang, X., Song, Z., Zong, C., Wei, N., Li, D., 2019b. Consistent transport of terrestrial microplastics to the ocean through atmosphere. Environ. Sci. Technol. 53, 10612–10619. https://doi.org/10.1021/acs.est.9b03427.
Liu, Y., Haussaire, J.M., Bocquet, M., Roustan, Y., Saunier, O., Mathieu, A., 2017. Uncertainty quantification of pollutant source retrieval: comparison of Bayesian methods with application to the Chernobyl and Fukushima Daiichi accidental releases of radionuclides. Q. J. R. Meteorol. Soc. 143, 2886–2901. https://doi.org/10.1002/qj.3138.
Materić, D., Ludewig, E., Brunner, D., Röckmann, T., Holzinger, R., 2021. Nanoplastics transport to the remote, high-altitude Alps. Environ. Pollut. 288. https://doi.org/10.1016/j.envpol.2021.117697.
Mattsson, K., Hansson, L.A., Cedervall, T., 2015. Nano-plastics in the aquatic environment. Environ. Sci. Process. Impacts 17, 1712–1721. https://doi.org/10.1039/c5em00227c.
Mountford, A.S., Morales Maqueda, M.A., 2021. Modeling the accumulation and transport of microplastics by sea ice. J. Geophys. Res. Ocean 126, 1–19. https://doi.org/10.1029/2020JC016826.
Nizzetto, L., Futter, M., Langaas, S., 2016. Are agricultural soils dumps for microplastics of urban origin? Environ. Sci. Technol. 50, 10777–10779. https://doi.org/10.1021/acs.est.6b04140.
O'Brien, S., Okoffo, E.D., O'Brien, J.W., Ribeiro, F., Wang, X., Wright, S.L., Samanipour, S., Rauert, C., Toapanta, T.Y.A., Albarracin, R., Thomas, K.V., 2020. Airborne emissions of microplastic fibres from domestic laundry dryers. Sci. Total Environ. 747, 141175 https://doi.org/10.1016/j.scitotenv.2020.141175.
O'Brine, T., Thompson, R.C., 2010. Degradation of plastic carrier bags in the marine environment. Mar. Pollut. Bull. 60, 2279–2283. https://doi.org/10.1016/j.marpolbul.2010.08.005.
Parzen, E., 1962. On the estimation of probability density functions and mode. Ann. Math. Stat. 33, 1065–1076.
Patil, S., Bafana, A., Naoghare, P.K., Krishnamurthi, K., Sivanesan, S., 2021. Environmental prevalence, fate, impacts, and mitigation of microplastics—a critical review on present understanding and future research scope. Environ. Sci. Pollut. Res. 28, 4951–4974. https://doi.org/10.1007/s11356-020-11700-4.
Peeken, I., Primpke, S., Beyer, B., Gütermann, J., Katlein, C., Krumpen, T., Bergmann, M., Hehemann, L., Gerdts, G., 2018. Arctic sea ice is an important temporal sink and means of transport for microplastic. Nat. Commun. 9. https://doi.org/10.1038/s41467-018-03825-5.
Peñalver, R., Costa-Gómez, I., Arroyo-Manzanares, N., Moreno, J.M., López-García, I., Moreno-Grau, S., Córdoba, M.H., 2021. Assessing the level of airborne polystyrene microplastics using thermogravimetry-mass spectrometry: results for an agricultural area. Sci. Total Environ. 787, 1–8. https://doi.org/10.1016/j.scitotenv.2021.147656.
Penkała, M., Ogrodnik, P., Rogula-Kozłowska, W., 2018. Particulate matter from the road surface abrasion as a problem of non-exhaust emission control. Environments 5, 9. https://doi.org/10.3390/environments5010009.
Piehl, S., Leibner, A., Löder, M.G.J., Dris, R., Bogner, C., Laforsch, C., 2018. Identification and quantification of macro- and microplastics on an agricultural farmland. Sci. Rep. 8, 1–9. https://doi.org/10.1038/s41598-018-36172-y.
Pisso, I., Sollum, E., Grythe, H., Kristiansen, N., Cassiani, M., Eckhardt, S., Arnold, D., Morton, D., Thompson, R.L., Groot Zwaaftink, C.D., Evangeliou, N., Sodemann, H., Haimberger, L., Henne, S., Brunner, D., Burkhart, J.F., Fouilloux, A., Brioude, J., Philipp, A., Seibert, P., Stohl, A., 2019. The Lagrangian particle dispersion model FLEXPART version 10.4. Geosci. Model Dev. 12, 4955–4997. https://doi.org/10.5194/gmd-12-4955-2019.

PlasticsEurope, 2019. Plastics - the Facts 2019 [WWW Document]. URL ⟨https://www.plasticseurope.org/en/resources/market-data⟩ (accessed 5.12.20).
Qian, J., Ferro, A.R., 2008. Resuspension of dust particles in a chamber and associated environmental factors. Aerosol Sci. Technol. 42, 566–578. https://doi.org/10.1080/02786820802220274.
Ragusa, A., Svelato, A., Santacroce, C., Catalano, P., Notarstefano, V., Carnevali, O., Papa, F., Rongioletti, M.C.A., Baiocco, F., Draghi, S., D'Amore, E., Rinaldo, D., Matta, M., Giorgini, E., 2021. Plasticenta: First evidence of microplastics in human placenta. Environ. Int. 146, 106274 https://doi.org/10.1016/j.envint.2020.106274.
Ramankutty, N., Evan, A.T., Monfreda, C., Foley, J.A., 2008. Farming the planet: 1. Geographic distribution of global agricultural lands in the year 2000. Global Biogeochem. Glob. BioCycles 22, 1–19. https://doi.org/10.1029/2007GB002952.
Revell, L.E., Kuma, P., Ru, E.C., Somerville, W.R.C., Gaw, S., 2021. Direct radiative effects of airborne microplastics. Nature 598. https://doi.org/10.1038/s41586-021-03864-x.
Roblin, B., Ryan, M., Vreugdenhil, A., Aherne, J., 2020. Ambient atmospheric deposition of anthropogenic microfibers and microplastics on the western periphery of Europe (Ireland). Environ. Sci. Technol. 54, 11100–11108. https://doi.org/10.1021/acs.est.0c04000.
Rogge, W.F., Hildemann, L.M., Mazurek, M.A., Cass, G.R., Simoneit, B.R.T., 1993. Sources of fine organic aerosol. 3. road dust, tire debris, and organometallic brake lining dust: roads as sources and sinks. Environ. Sci. Technol. 27, 1892–1904. https://doi.org/10.1021/es00046a019.
Royer, S.-J., Ferron, S., Wilson, S.T., Karl, D.M., 2018. Production of methane and ethylene from plastic in the environment. PLoS One 13, e0200574. https://doi.org/10.1371/journal.pone.0200574.
Schwabl, P., Koppel, S., Konigshofer, P., Bucsics, T., Trauner, M., Reiberger, T., Liebmann, B., 2019. Detection of various microplastics in human stool: a prospective case series. Ann. Intern. Med. 171, 453–457. https://doi.org/10.7326/M19-0618.
Scott, D.W., 2015. Multivariate density estimation: Theory, practice, and visualization: Second edition, Multivariate Density Estimation: Theory, Practice, and Visualization: Second Edition. https://doi.org/10.1002/9781118575574.
Seibert, P., Frank, A., 2004. Source-receptor matrix calculation with a Lagrangian particle dispersion model in backward mode. Atmos. Chem. Phys. 4, 51–63. https://doi.org/10.5194/acp-4-51-2004.
Sharma, S., Chatterjee, S., 2017. Microplastic pollution, a threat to marine ecosystem and human health: a short review. Environ. Sci. Pollut. Res. 24, 21530–21547. https://doi.org/10.1007/s11356-017-9910-8.
Smidl, V., Quinn, A., 2006. The Variational Bayes Method in Signal Processing. Springer, Berlin Heidelberg New York.
Sommer, F., Dietze, V., Baum, A., Sauer, J., Gilge, S., Maschowski, C., Gieré, R., 2018. Tire abrasion as a major source of microplastics in the environment. Aerosol Air Qual. Res. 18, 2014–2028. https://doi.org/10.4209/aaqr.2018.03.0099.
Sørensen, J.H., Bartnicki, J., Blixt Buhr, A.M., Feddersen, H., Hoe, S.C., Israelson, C., Klein, H., Lauritzen, B., Lindgren, J., Schönfeldt, F., Sigg, R., 2020. Uncertainties in atmospheric dispersion modelling during nuclear accidents. J. Environ. Radioact. 222. https://doi.org/10.1016/j.jenvrad.2020.106356.
Stanton, T., Johnson, M., Nathanail, P., MacNaughtan, W., Gomes, R.L., 2019. Freshwater and airborne textile fibre populations are dominated by 'natural', not microplastic, fibres. Sci. Total Environ. 666, 377–389. https://doi.org/10.1016/j.scitotenv.2019.02.278.
Stohl, A., Forster, C., Frank, A., Seibert, P., Wotawa, G., 2005. Technical note: the Lagrangian particle dispersion model FLEXPART version 6.2. Atmos. Chem. Phys. 5, 2461–2474. https://doi.org/10.5194/acp-5-2461-2005.
Syafei, A.D., Nurasrin, N.R., Assomadi, A.F., Boedisantoso, R., 2019. Microplastic pollution in the ambient air of Surabaya, Indonesia. Curr. World Environ. 14, 290–298. https://doi.org/10.12944/cwe.14.2.13.
Szewc, K., Graca, B., Dołęga, A., 2021. Atmospheric deposition of microplastics in the coastal zone: characteristics and relationship with meteorological factors. Sci. Total Environ. 761, 143272 https://doi.org/10.1016/j.scitotenv.2020.143272.
Szymańska, M., Obolewski, K., 2020. Microplastics as contaminants in freshwater environments: a multidisciplinary review. Ecohydrol. Hydrobiol. 20, 333–345. https://doi.org/10.1016/j.ecohyd.2020.05.001.
Tichý, O., Šmídl, V., Hofman, R., Stohl, A., 2016. LS-APC v1.0: A tuning-free method for the linear inverse problem and its application to source-term determination. Geosci. Model Dev. 9, 4297–4311. https://doi.org/10.5194/gmd-9-4297-2016.
Tichý, O., Ulrych, L., Šmídl, V., Evangeliou, N., Stohl, A., 2020. On the tuning of atmospheric inverse methods: comparisons with the European Tracer Experiment (ETEX) and Chernobyl datasets using the atmospheric transport model FLEXPART. Geosci. Model Dev. 13, 5917–5934. https://doi.org/10.5194/gmd-13-5917-2020.
Tipping, M.E., 2001. Sparse Bayesian learning and the relevance vector machine. J. Mach. Learn. Res. 1, 211–244. https://doi.org/10.1162/15324430152748236.
Trainic, M., Flores, J.M., Pinkas, I., Pedrotti, M.L., Lombard, F., Bourdin, G., Gorsky, G., Boss, E., Rudich, Y., Vardi, A., Koren, I., 2020. Airborne microplastic particles detected in the remote marine atmosphere. Commun. Earth Environ. 1, 1–9. https://doi.org/10.1038/s43247-020-00061-y.
Truong, T.N.S., Strady, E., Kieu-Le, T.C., Tran, Q.V., Le, T.M.T., Thuong, Q.T., 2021. Microplastic in atmospheric fallouts of a developing Southeast Asian megacity under tropical climate. Chemosphere 272, 129874. https://doi.org/10.1016/j.chemosphere.2021.129874.
Tunahan Kaya, A., Yurtsever, M., Çiftçi Bayraktar, S., 2018. Ubiquitous exposure to microfiber pollution in the air. Eur. Phys. J. 133. https://doi.org/10.1140/epjp/i2018-12372-7.
Wagner, S., Hüffer, T., Klöckner, P., Wehrhahn, M., Hofmann, T., Reemtsma, T., 2018. Tire wear particles in the aquatic environment - a review on generation, analysis, occurrence, fate and effects. Water Res. 139, 83–100. https://doi.org/10.1016/j.watres.2018.03.051.
Wagner, S., Reemtsma, T., 2019. Things we know and don't know about nanoplastic in the environment. Nat. Nanotechnol. 14, 300–301. https://doi.org/10.1038/s41565-019-0424-z.
Wang, J., Zheng, L., Li, J., 2018. A critical review on the sources and instruments of marine microplastics and prospects on the relevant management in China. Waste Manag. Res. 36, 898–911. https://doi.org/10.1177/0734242X18793504.
Wang, X., Li, C., Liu, K., Zhu, L., Song, Z., Li, D., 2020. Atmospheric microplastic over the South China Sea and East Indian Ocean: abundance, distribution and source. J. Hazard. Mater. 389, 121846 https://doi.org/10.1016/j.jhazmat.2019.121846.
Wang, X., Liu, K., Zhu, L., Li, C., Song, Z., Li, D., 2021. Efficient transport of atmospheric microplastics onto the continent via the East Asian summer monsoon. J. Hazard. Mater. 414, 125477 https://doi.org/10.1016/j.jhazmat.2021.125477.
Weiss, L., Ludwig, W., Heussner, S., Canals, M., Ghiglione, J.F., Estournel, C., Constant, M., Kerhervé, P., 2021. The missing ocean plastic sink: gone with the rivers. Science 373, 107–111. https://doi.org/10.1126/science.abe0290.
Wilcox, C., Puckridge, M., Schuyler, Q.A., Townsend, K., Hardesty, B.D., 2018. A quantitative analysis linking sea turtle mortality and plastic debris ingestion. Sci. Rep. 8, 1–11. https://doi.org/10.1038/s41598-018-30038-z.
World Economic Forum, 2016. The New Plastics Economy: Rethinking the future of plastics. Ellen MacArthur Foundation.
Wright, S.L., Kelly, F.J., 2017. Plastic and human health: a micro issue? Environ. Sci. Technol. 51, 6634–6647. https://doi.org/10.1021/acs.est.7b00423.
Wright, S.L., Ulke, J., Font, A., Chan, K.L.A., Kelly, F.J., 2020. Atmospheric microplastic deposition in an urban environment and an evaluation of transport. Environ. Int. 136, 105411 https://doi.org/10.1016/j.envint.2019.105411.
Yukioka, S., Tanaka, S., Nabetani, Y., Suzuki, Y., Ushijima, T., Fujii, S., Takada, H., Van Tran, Q., Singh, S., 2020. Occurrence and characteristics of microplastics in surface road dust in Kusatsu (Japan), Da Nang (Vietnam), and Kathmandu (Nepal). Environ. Pollut. 256, 113447 https://doi.org/10.1016/j.envpol.2019.113447.
Zhang, Q., Xu, E.G., Li, J., Chen, Q., Ma, L., Zeng, E.Y., Shi, H., 2020. A review of microplastics in table salt, drinking water, and air: direct human exposure. Environ. Sci. Technol. 54, 3740–3751. https://doi.org/10.1021/acs.est.9b04535.
Zhao, Y.B., Gao, P.P., Ni, H.G., 2019. A chemical time bomb: future risks of microplastics. Water Air Soil Pollut. 230. https://doi.org/10.1007/s11270-019-4320-9.
Zhou, Q., Tian, C., Luo, Y., 2017. Various forms and deposition fluxes of microplastics identified in the coastal urban atmosphere. Chin. Sci. Bull. 62, 3902–3909. https://doi.org/10.1360/N972017-00956.
Zhu, X., Huang, W., Fang, M., Liao, Z., Wang, Y., Xu, L., Mu, Q., Shi, C., Lu, C., Deng, H., Dahlgren, R., Shang, X., 2021. Airborne microplastic concentrations in five megacities of Northern and Southeast China. Environ. Sci. Technol. https://doi.org/10.1021/acs.est.1c03618.